Nanoindentation of Thin Films and Plasma Treated Surfaces

Editors: V. Buršíková , Anna Campbell Charvátová, Petr Klapetek

Brno, 20. 12. 2019

Contents

Preface

In the last quarter of the 20th century there has been a very considerable increase in the use of indentation techniques for determining the mechanical properties of solids [Joh85, DN86, BR87]. The indentation technique became one of the most commonly used methods to provide the mechanical characteristics (hardness, yield stress, Young's modulus, fracture toughness, adhesion and cohesion, and others) of the thin films [Mat86,JRL89,GAM81, GS78,MOGC92].

Among the large range of existing methods, the Vickers test using a diamond pyramid indenter is one in most widespread use [For94, A.E94, ZR96].

Recently the depth sensing indentation (DSI) method became a widely used method of hardness determination. In the case of the DSI tester the applied load is registered as a function of indentation depth both during loading and unloading. This method enables to determine the elastic and plastic part of the indentation work, the elastic modulus, the hardness, the compressive yield stress of the films etc. [OP92b, GMPB92].

However, in order to measure the true hardness of coatings, it is important to find the critical testing condition under which the substrate does not influence the measurement. The critical penetration depths, reported in the past [JH84,MM94,MK96] are widely scattered according to the investigators and the combinations of the coatings and the substrates. In order to obtain reliable values of mechanical properties of coatings, it is important to find the cause of this wide scatter of the critical penetration depth.

In addition, there are fundamental problems relating to the effects of the friction between the indenter and the coating surface. Atkinson and Shi [MA89] have pointed out through Vickers indentation tests conducted with and without a lubricant that friction is the principal factor causing load-dependence of the hardness values. That is, the effects of friction should be taken into account to analyse load-displacement response of coating materials [MK96].

Indentation by a sharp indenter introduces a three-dimensional (3D) stress field under the indenter, associated with plastic and elastic deformation during loading. The indentation stress field is generally characterised as

elastic-plastic [Mar64,Joh85,SCE82], based on the expanded spherical cavity solution [Hil50] . In recent years, various FEM analyses have been made of the stress fields created by sharp indenter.

Laursen and Simo [LS92] and Ritter have pointed out through their numerical simulations of the indentation processes of thin coatings that the finite-element method (FEM) provides a tool that enables better understanding of the mechanics involved in indentation. They have found that the indentation behaviour is significantly influenced by the coating-substrate combinations. The recent FEM models are 3D and include the effects of the indenter shape, strain hardening and pressure sensitivity.

Indentation hardness has been extensively developed in the last years to study the hardness of carefully prepared polished surfaces and of the surface films, the influence of specimen and indentation size, the creep of solids and the fracture of the brittle solids.

Since the development of very low load indentation hardness machines and the invention of the scanning tunnelling and atomic force microscopes (STM, AFM), hardness studies have been routinely possible on the nanometer scale [SD99]. AFM allows to analyse mechanical and tribological properties of the surface and near surface of thin films due to the low applied loads compared with other techniques. The different modes of AFM operation, such as contact mode, force modulation, lateral force and force-distance curve, provide information on wear, relative hardness, friction, tip surface adhesion, surface stiffness and Young's modulus.

However, in spite of the numerous applications of the micro- and nanoindentation techniques, the mechanical and physical processes involved and related physico-chemical phenomena are not yet fully understood.

Part I

Mechanical properties

Chapter 1

Mechanical properties in general

V. Buršíková
Department of Physical Electronics, Faculty of Science, Masaryk University, Kotlářská 2, 611 37 Brno, Czech Republic

1.1 Basic terms

The term mechanical properties of materials includes, in the ordinary sense, elasticity, plasticity, ductility, creep resistance, strength, hardness, toughness and brittleness. These terms require clear definitions according to which it will be possible to propose methods for their determination and numerical evaluation.

1.1.1 Stress and strain

When testing materials, we study the response of the material to acting of external forces. When the material is subjected to a static external stress, the atoms constituting the material are rearranged so as to maintain a balance between the external forces acting and the interatomic forces. Macroscopically, the rearrangement of atoms manifests itself as a strain. In order to obtain general relationships, we first have to eliminate the influence of material dimensions. To do so, we refer to the external forces occurring per unit of stressed cross-section. The load on the unit cross-section is called *stress* and its unit is in the SI system Pa (Pascal) $[\mathrm{P}a = N/m^2]$. External forces are contradicted by internal forces, the nature of which will be described later. In order to compare dimensional changes in deformation of

different bodies, we need to introduce dimensionless quantities expressing the relative change in dimensions of deformed bodies. For example, in the case of an uniaxial elongation, we can introduce a quantity called the nominal elongation ε corresponding to the change in length Δl of the original length l_o.

$$\varepsilon = \frac{\Delta l}{l_o} \tag{1.1}$$

ε is also called as *engineering strain*. The change in length d1 may also be related to the instantaneous length of the deformed body according to the following relationship:

$$\varepsilon_t = \int_{l_o}^{l} \frac{\mathrm{d}l}{l} = \ln(1+\varepsilon). \tag{1.2}$$

In this case, we are talking about the "true" proportional extension: *true strain*.

The nominal relative elongation (engineering strain) ε is usually related to the nominal stress σ corresponding to the initial cross- section of the stressed body A_o, while the true elongation (true strain) is related to the *true stress*, σ_t i.e. the stress corresponding to the instantaneous cross-section A.

1.1.2 Elasticity

We perceive the meaning of *elasticity* intuitively: We consider a material to be ideally elastic if it deforms under the influence of external forces but immediately returns to its original state when they are removed. On the other hand, the ideally inelastic (perfectly plastic) material changes its shape due to the external forces and it remains deformed even after the removal. In the case if we want to quantify the elasticity of materials, we need two parameters. First, we need to determine the maximum stress up to which the material deforms only elastically. This limit stress is called the elastic limit. Secondly, we need to know the relationship between the magnitude of the acting external force and the magnitude of the resulting elastic deformation. According to 17. century English physicist, Robert Hooke, for a large number of materials (especially metals) there is a direct proportionality between the stress and the deformation caused by it. The elastic deformation takes place at the moment of applying the stress and disappears when the applied stress is removed. This deformation is therefore time independent and reversible. The constant of proportionality between stress and relative deformation is called the modulus of elasticity. We distinguish the modulus of elasticity in tension E and shear G.

1.1.3 Strength

The strength of materials (unit: Pa) characterises the material ability to resist against permanent deformation. Again we perceive the meaning of the strength intuitively, however its quantification is more complicated. In metals the permanent deformation starts at so called *yield*stress, when dislocations first move large distances. The material strength is determined from the stress-strain curve. Determination of the start of yielding is difficult, therefore in case of metals we identify the stress at which the stress-strain curve for axial loading deviates by a strain of 0.2% from the linear-elastic line. For polymers, the strength is identified as the stress at which the stress-strain curve becomes markedly non-linear: typically, a strain of 1 %. This may be caused by the irreversible slipping of molecular chains (shear-yielding), or it may be caused by the formation of low density, crack-like volumes (crazing).

1.1.4 Fracture Strength

The fracture strength (unit: Pa) is defined as the largest stress required to separate the material into two parts. According to the way of the separation we distinguish between tensile, compressive, bending and torsional strength. Unless otherwise stated, the term strength always means tensile strength. If the force P_{max}, which caused the separation, and the size of the original cross-section A_o at the separation are known, the tensile strength is expressed as follows:

$$\tau = \frac{P_{max}}{A_0} \tag{1.3}$$

This relationship is an expression of the so-called nominal or conventional strength. As we mentioned in the previous section, the true stress at any point in the test will be different from the stress related to the original cross section A_o. It is therefore necessary to distinguish between the nominal (engineering) maximum stress and the true maximum stress.

1.1.5 Ductility

The ductility is a measure of how much strain a given stress produces. Highly ductile metals can exhibit significant strain before fracturing, whereas brittle materials frequently display very little strain. An overly simplistic way of viewing ductility is the degree to which a material is â€śforgivingâ€ť of local deformation without the occurrence of fracture.

There are two measures of the ductility:

- Percent Elongation (%El) $\%El = \frac{l-l_0}{l_0} x100$

- Percent Reduction In Area $\%RA = \frac{Al - A_0}{A_0} x100$

Ductility measures the amount of plastic deformation that a material goes through by the time it breaks.

Brittle materials:$\%EL < 5\%$ at fracture
Ductile materials: $\%EL$ and $\%RA$ both $> 25\%$
Ductility is a measure of how much strain a given stress produces. Highly ductile metals can exhibit significant strain before fracturing, whereas brittle materials frequently display very little strain. An overly simplistic way of viewing ductility is the degree to which a material is able to undergo local deformation without the occurrence of fracture.

1.1.6 Resilience

The resilience is the ability of material to absorb energy during elastic deformation. It measures the maximum energy stored elastically without any damage to the material, and which is released again on unloading. It is possible to express it quantitatively using the modulus of resilience, U_r (units J/m^3). U_r is the area under the stress-strain curve:

$$U_r = \int_0^{\varepsilon} \sigma \, \mathrm{d}\varepsilon. \tag{1.4}$$

If we assume a linear elastic region, then we may express the resilience as

$$U_r = \frac{1}{2}\sigma\varepsilon = \frac{1}{2}\sigma\frac{\sigma}{E} = \frac{\sigma^2}{E} \tag{1.5}$$

1.1.7 Toughness and Fracture Toughness

The toughness K_t may be defined similarly as the resilience: it is the area under stress-strain curve up to fracture (units J/m^3).

$$K_t = \int_0^{\varepsilon_f} \sigma \, \mathrm{d}\varepsilon, \tag{1.6}$$

where ε_f is the deformation up to fracture.

The fracture toughness, K_{Ic}, (units: $\mathrm{MPam}^{\frac{1}{2}}$) is the measure of the resistance of the material to the propagation of a crack. The quantity K_{Ic}, is calculated from the following formulae:

$$K_{Ic} = K_Y \frac{\sigma_c}{\sqrt{\pi c}}, \tag{1.7}$$

where K_Y is a geometric factor near unity, σ_c is the stress causing the propagation of the crack with crack length c. The toughness may be expressed on the basis of the previous formulae as

$$G_c = \frac{K_{Ic}^2}{E(l+\nu)} \tag{1.8}$$

The above defined values are well-defined for brittle materials (ceramics, glasses). In ductile materials a plastic zone develops at the crack tip and it is more complicated to define their fracture toughness.

1.1.8 Wear Resistance

The wear resistance is not a bulk phenomena, it involves interactions between two materials, between the material of the tester and the material of the tested sample. The wear resistance is characterised by wear rate, which is the volume of the lost material per unite area from the tested material surface. The wear rate of the material surface is characterized by the

Archard wear constant, k_A (unit: Pa^{-1}) [?], defined by the following equation W

$$\frac{W}{A} = k_A p, \tag{1.9}$$

where A is the area of the tested material surface and p the pressure (i.e. force per unit area) pressing the tested material and the tester together. This value must be interpreted as the property of the sliding couple, without knowing the tester material it makes no sense.

Acknowledgement This research was funded by the Ministry of Education, Youth and Sports of the Czech Republic, project LO1411 (NPU I) and by by Czech Science Foundation project No. 15-17875S [1]

[1]Submitted: 31.7.2018; Accepted: 20.12.2019

Chapter 2

Elastic Parameters

V. Buršíková
Department of Physical Electronics, Faculty of Science, Masaryk University, Kotlářská 2, 611 37 Brno, Czech Republic

The most common test that is used to determine the proportionality constant between stress and strain is the uniaxial tensile test. If we stretch a cylindrical bar with a diameter of d_0, a cross-sectional area of A_0 and a length of l_0 below the elastic limit, its length will increase in proportion to the stress. Let the bar length increase at P to l. The relation between the nominal stress $\sigma = \frac{4P}{pid^2}$ and the nominal relative deformation $\varepsilon = \frac{l-l_0}{l_0}$ is expressed by the equation

$$E = \frac{\sigma}{\varepsilon}. \tag{2.1}$$

The proportionality constant E is called Young's modulus after the English scientist Thomas Young, who introduced the concept of elastic modulus in 1802.

As the length of the stretched rod increases, at the same time its diameter decreases from d_0 to d. The relative reduction in diameter is

$$\kappa = \frac{d_o - d}{d_0} \tag{2.2}$$

and Hook's law of proportionality with tension also applies to him. The ratio of both variables of elastic deformation is called Poisson ratio

$$\nu = \frac{\kappa}{\varepsilon}. \tag{2.3}$$

The designation was chosen according to the French physicist S.D. Poisson, who introduced this value.

The Poisson ratio is an important value for various computations in the field of elasticity. It is easy to calculate the volume change caused by the elastic tension. The original volume of the rod is

$$V_0 = \frac{\pi {d_0}^2}{4} l_0, \tag{2.4}$$

and the volume after elastic tensile deformation is

$$V = \frac{\pi {d_0}^2}{4} l. \tag{2.5}$$

The change of the volume is

$$\Delta V = V - V_0. \tag{2.6}$$

By substituting into the above mentioned relations, we get to the approximate formula by neglecting the quadratic term

$$\frac{\Delta V}{V} \simeq \varepsilon(1 - 2\nu). \tag{2.7}$$

Since simple tensile loading increases, the right side must have a positive value and hence the Poisson ratio must be equal or less than 0.5.

$$\varepsilon(1 - 2\nu) \geqslant 0 \Longrightarrow \nu \leq 0.5. \tag{2.8}$$

The constitutive relation (Hooke's law) relates the applied stress to the resulting strain:

$$\epsilon_{ij} = S_{ijkl}\sigma_{kl} \tag{2.9}$$

$$\sigma_{ij} = C_{ijkl}\epsilon_{kl} \tag{2.10}$$

Here σ_{ij} and ϵ_{kl} are the components of the stress tensor and the strain tensor, respectively. Both of them are tensors of the second order.

The diagonal components σ_{ii} of the stress tensor are called *normal stresses* and the off-diagonal ones $\sigma_{ij}, i \neq j$ are called the tangential or *shear stresses*. By an appropriate change of the coordinates a given stress tensor may always be put under the diagonal form, where the only non-zero terms are the diagonal ones. So the *principal stresses* σ_{11}, σ_{22}, σ_{33} are obtained.

The *hydrostatic pressure* P is the the one third of the sum of the principal stresses (one third of the trace of the stress tensor): $P = \frac{1}{3}(\sigma_{11} + \sigma_{22} + \sigma_{33})$.

The components of tensors of the forth order, S_{ijkl} and C_{ijkl} are the so called *elastic moduli* and *elastic coefficients*, respectively. This coefficients

Material	**Poisson's Ratio**
Al	0.33
Al_2O_3	0.231
Aluminum alloys	0.330–0.334
Acrylonitrile butadiene styrene (ABS)	0.35
Brass, 70–30	0.331
Brass, cast	0.357
Bronze	0.34
Boronsilicate glass BK7	0.20
Concrete	0.15 - 0.20
Copper, pure	0.34
Cu-Zr-Be glass	0.35–0.39
clay	0.30–0.45
C (graphite)	0.31
Diamond	0.07
glass	0.18–0.3
Glass ceramic (machinable)	0.29
gold	0.42–0.44
Iron	0.291
Cast Iron	0.211 – 0.299
Iron, ductile	0.26 - 0.31
Iron, malleable	0.271
Lead, pure	0.40 - 0.45
Magnesium	0.35
Molybdenum, wrought	0.32
Nickel, pure	0.31
Nylon (0.2 wt%)	0.34–0.43
Platinum	0.39
Polycarbonate	0.37
Polymethyl methacrylate	0.365–0.375
Polyethylene terephtalate	0.29
Polyvinyl chloride	0.38
Polytetrafluoroethylene	0.41–0.42
Quartz	0.17
Rubber (natural)	0.4999
Silver, pure	0.37
Steel, AISI C1020 (hot-worked)	0.29
AISI 1025 Carbon Steel	0.32
17-7PH Stainless Steel	0.28
17-4PH Stainless Steel	0.27
TiN	0.25
Tin, commercially pure	0.33
99.2 Ti (ASTM grade 2)	0.34
Titanium Alloy (Ti-8Al-1Mo-1V)	0.32
Titanium Alloy (Ti-6Al-4V)	0.34
Ti_3SiC_2	0.20
Tungsten	0.28
Zinc (Commercially pure)	0.25

Table 2.1: Examples of Poisson's ratio numbers for some pure elements [12–19], engineering alloys [13,16, 20–25], polymers [26–31] and ceramics [32–45].

are depending on the material properties. In the case of the isotropic body, the elastic constant are reduced only to two constants. The Eq. 2.10 is then possible to express using the so called Lamé's constants, λ and G

$$\sigma_{ij} = \lambda\delta_{ij}\sum_{k}^{3}\epsilon_{kk} + 2G\epsilon_{ij} \tag{2.11}$$

where

$$\begin{aligned} \delta_{ij} &= 1 \quad for \quad i = j \\ \delta_{ij} &= 0 \quad for \quad i \neq j \\ \sum_{i}^{3}\epsilon_{ii} &= \Delta V/V \end{aligned} \tag{2.12}$$

and G is the shear modulus. The relationship between the elastic moduli describing the deformation of an isotropic body has the following form

$$\frac{1}{E} = \frac{1}{3G} + \frac{1}{9K} \tag{2.13}$$

Here E is the Young's modulus and K is the bulk modulus.

For practical use the first form of Hooke's law (Eq. 2.9) is more advantageous. That is easier to apply a simple stress, for example uniaxial stress, in specified direction and to measure all components of the strain tensor arised from the acting stress. The second form of the Hooke's law (Eq. 2.10) could be written in the following form

$$\epsilon_{ij} = -\frac{\nu}{E}\delta_{ij}\sum_{k}^{3}\sigma_{kk} + \frac{1+\nu}{E}\sigma_{ij} \tag{2.14}$$

where ν is the Poisson's ratio.

The Young's modulus E and the Poisson's ratio ν could be expressed with Lamés constants according to following equations

$$\nu = \frac{\lambda}{2(\lambda+G)} \tag{2.15}$$

$$E = \frac{G(3\lambda+2G)}{(\lambda+G)} \tag{2.16}$$

For *hydrostatic compression*, the useful elastic constant is the modulus of incompressibility or *bulk modulus*.

$$K = \frac{1}{\beta} = -V\frac{\mathrm{d}p}{\mathrm{d}V} = V\frac{\mathrm{d}^2U}{\mathrm{d}V^2} \tag{2.17}$$

where U is the internal energy.

Relation of the bulk modulus to the Lamè's coefficients is the following

$$K = \frac{1}{3}(3\lambda + 2G) \tag{2.18}$$

The bulk modulus K (??) is the reciprocal value of the compressibility β.

The compressibility β is the isothermal relative volume change of a body produced by the application of a hydrostatic pressure p:

$$\beta = -\frac{1}{V}\left(\frac{\partial V}{\partial p}\right)_T \tag{2.19}$$

Elastic coefficients C_{ijkl} are measures of the change of the bonding energy of the crystal subjected to elastic deformation at 0 K.

$$C_{ijkl} = \left(\frac{\partial^2 u}{\epsilon_{ij}\epsilon_{kl}}\right)_{r=r_0} \tag{2.20}$$

where u is the lattice energy per volume, r_0 is the bond length.

Acknowledgement This research was funded by the Ministry of Education, Youth and Sports of the Czech Republic, project LO1411 (NPU I) and by Czech Science Foundation project No. 15-17875S [1]

[1]Submitted: 31.7.2018; Accepted: 20.12.2019

Chapter 3

Hardness in General

V. Buršíková
Department of Physical Electronics, Faculty of Science, Masaryk University, Kotlářská 2, 611 37 Brno, Czech Republic

The hardness is defined as the resistance of a body against the intrusion of another harder and non-deforming object (indenter) during a local contact interaction. Hardness represents a complicated average of material properties. The measured hardness depends on the elastic and plastic properties of the material to be investigated. It depends also on the measuring technique applied and on the shape and nature of the indenter.

Moreover, the mechanical properties of materials in small dimensions can be very different from those of bulk material having the same composition. For example, thin films may have micro-structures not existing in the bulk materials. There is also the effect of the dimensional constraints when dimensions of the objects approach some characteristic length scale in the material (grain size, dislocation spacing, precipitate spacings)

Despite many attempts to develop a strong physical definition of hardness, thus also an absolute hardness scale, the theory of hardness has remained up to now semi-empirical. We need to have on mind, that *hardness is not a fundamental physical quantity!*

As a consequence, up to now it has also proven impossible to correlate the hardness of a material strongly to other material properties, although for individual classes of materials semi-empirical relationships have been developed between the hardness on the one hand and properties such as nature of the bonding, the bond strength, the bond length, etc. on the other hand. [Kul99]

On contrary, the closely related material properties as the compressibility

Method	Indenter	Definition	Notes
Brinell	Sphere	$H_B = \frac{2L}{\pi D(D-\sqrt{(D^2-d^2)}}$ D = sphere diameter, d = diameter of impression.	the measured hardness depends on the applied load.
Rockwell	Sphere, cone	The Rockwell hardness is the difference between the impression depth after indenting with low and high loads.	Depending on the form and material of the indenter (steel, diamond) and on the starting and final loads there are alltogether 18 Rockwell scales covering different ranges of hardness.
Vickers	Quadratic pyramid	$H_V = \frac{1.854L}{d^2}$, d = diameter of impression.	Owing to the form of the indenter, the hardness is independent of the applied load.
Knoop	Rhomboedral pyramid; ratio of diagonals 7:1	$H_K = \frac{14.2L}{l^2}$ l = length of the long diagonal of the impression.	Owing of the long diagonal this method has advantages with respect to the Vickers in the case of very hard coatings and low test loads.
Berkowitch	Triangular pyramid		Values are mostly 10-20% higher than Knoop hardness values.

Table 3.1: Survey of the different indenters used for hardness measurement and their description [Kul99]

β, the bulk modulus K and the tensile strength σ_{T}, have clear physical meanings. These properties are often used synonymously with "hardness" even if they have other physical meanings. Unlike the tensile strength and the compressibility of materials represent bulk properties, the hardness is a surface property.

The tensile strength σ_T is the maximum stress occurring during a tensile test, related to the original cross section of the body under test. Like hardness, it depends in a complex manner on the elastic and plastic properties of the material, nevertheless, one can at least derive a theoretical value of tensile strength of ideal materials.

The following Table 3.1 gives the survey of several different indenters and shows the differences in hardness measures obtained with that particular indenters.

The oldest hardness scale was introduced by Mohs. According to Mohs,

No	Mohs	Material	Chemical formulae	Hardness [GPa]
1	**1**	**Talc**	$Mg_2Si_4O_10.Mg(OH)_2$	0.02 - 0.10
2	**2**	**Gypsum**	$CaSO_4.2H_2O$	0.3 - 0.8
3		Salt	NaCl	0.3 - 0.9
4	**3**	**Calcite**	$CaCO_3$	0.6 - 1.0
5		Galenite	PbS	1.1 - 1.5
6	**4**	**Fluorite**	CaF_2	1.6 - 2.6
7	**5**	**Apatite**	$Ca_5(PO_4)_3(Cl,F,OH)$	2.5 - 5.4
8		Scheelite	$CaWO_4$	5.5 - 7.0
9	**6**	**Orthoclase**	$KAlSi_3O_8$	4.5 - 7.1
10		Magnetite	Fe_3O_4	6.0 - 8.5
11	**7**	**Quartz**	α-SiO_2	10.0 - 12.5
12	**8**	**Topaz**	$Al_2Fe(OH)_4SiO_4$	14.0 - 18.0
13		Tungsten carbide	WC	17.5 - 18.5
14	**9**	**Corundum**	α-Al_2O_3	20 - 24
15		Titanium carbide	TiC	30 - 34
16		Boron	B	34 - 36
17		Silicium carbide	SiC	38 - 41
18		Boron carbide	$B_{12}C_3$-$B_{13}C_2$	40 - 48
19		cubic boron nitride	β-BN	70 - 80
20		Diamond-carbonado	C	80 - 90
21	**10**	**Diamond natural (bort)**	C	90 - 100

Table 3.2: Comparison of the Mohs hardness scale (highlighted by bold typing) with the newest one including the novel superhard materials

the solid is harder than another if it can scratch this other material. In Table ?? the materials of Mohs scale are highlighted by bold typing. The Mohs hardnesses cover the region up to $H_V \approx 24$ GPa, whereas all harder materials are classified between order 9 and 10. However, these materials can posses Vickers hardnesses up to 100 GPa. The Mohs scale has therefore been extended in the upper region for example as it is shown in Table ??.

3.1 Relation of the uniaxial yield strength and the Young's modulus to the hardness

3.1.1 Two principal modes of the deformation under an indenter

It is possible to distinguish two principal modes of the deformation under an indenter:

a) The first is applicable to materials of low values of $\frac{\sigma_y}{E}$ where σ_y is the uniaxial compressive yield strength and E is the Young's modulus and includes mostly non-work-hardened metals. This mode was initially described by Tabor [Tab50] and closely follows the results of slip line field theory for a rigid-plastic material

$$\frac{H}{\sigma_y} \approx 3 \tag{3.1}$$

The important feature is that this materials becomes "piled-up" on either side of the indenter. (see Fig. 3.1)

b) For materials with higher$\frac{\sigma_y}{E}$ ratios (including work-hardened metals, ceramics and glasses) no surface displacements are apparent and the material removed from the indentation is accommodated by radial displacements. However, Tabor's equation no longer holds for materials with higher $\frac{\sigma_y}{E}$ ratios. Using the results for an expanding spherical cavity, Marsh [Mar64] proposed that the relationship between the hardness and yield stress in such cases may be represented by

$$\frac{H}{\sigma_y} \approx 0.28 + 0.6\left\{\frac{3}{3-\zeta} ln\left(\frac{3}{\zeta + 3\mu - \zeta\mu}\right)\right\} = A + BlnZ \tag{3.2}$$

where

$$\zeta = \frac{(1-2\nu)\sigma_y}{E}$$

$$\mu = \frac{(1+\nu)\sigma_y}{E}$$

and ν is the Poisson ratio.

Plotting $\frac{H}{\sigma_y}$ against $BlnZ$, Marsh found that a wide range of materials obeyed this equation. Such a plot is shown in 3.3 together with ranges of $BlnZ$.

A further result from the spherical cavity analysis is that the size of the hemispherical plastic zone is related to the size of the Vickers indentation according to

$$\frac{b}{a} = c\left(\frac{E}{H}\right)^{\frac{1}{2}} cot^{\frac{1}{3}}\phi \tag{3.3}$$

where a is the indentation semi-diagonal, b is the plastic zone radius, c is a constant approximatively equal to unity and ϕ is the indenter semi-angle (74^o) (See Fig. ??).

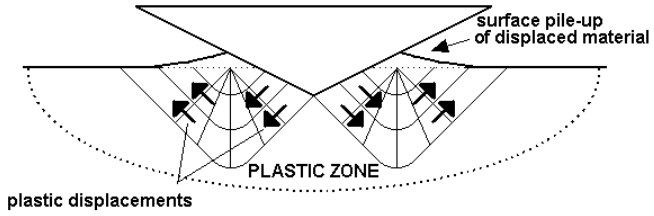

Figure 3.1: a)Low values of $\frac{\sigma_Y}{E}$

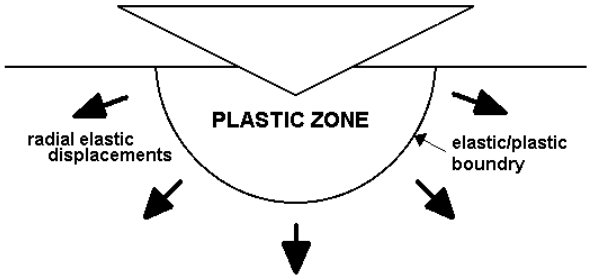

Figure 3.2: b)H igh values of $\frac{\sigma_Y}{E}$

3.2 The theoretical tensile strength and the theoretical critical shear stress

3.2.1 Ideal Materials

There is a close relation between the surface property, hardness, and the bulk property, tensile strength. The plastic deformation, in the case of the ductile materials, is the result of the movement of dislocations. On the other hand, the brittle failure is caused by the propagation of cracks. The theoretical tensile strength is given by

$$\sigma_{max} = \sqrt{\frac{E\gamma}{r_0}} \tag{3.4}$$

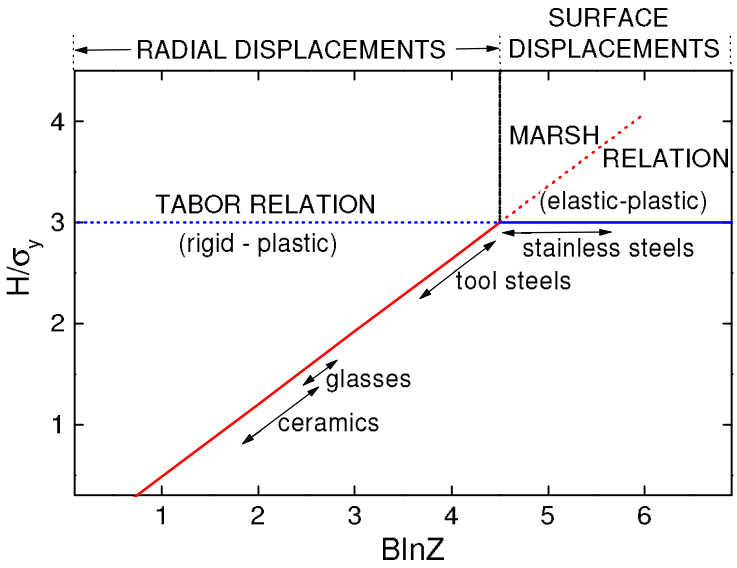

Figure 3.3: Plotting of $\frac{H}{\sigma_y}$ as a function of $BlnZ$ according to Eq. 3.2 [BR87]

Type of bond	σ_{max}	τ_{max}
Ionic	Low owing to long-range repulsive forces	High
Metallic	High	Low owing to the non-directional nature of bonds
Covalent	High	High

Table 3.3: Theoretical tensile strength σ_{max} and theoretical critical shear stress τ_{max} for the principal types of materials. The term "high" should be taken to imply only that there are no limitations in principle [Kul99].

It can be seen that the higher the Young's modulus E and the surface free energy γ and the lower the inter-atomic spacing r_0 of a material are, the higher σ_{max} is. These properties, however, are not independent of each other but strongly correlated.

In analogy the theoretical critical shear stress τ_{max} is

$$\tau_{max} = \frac{G a_0}{2\pi h_0} \tag{3.5}$$

where a_0 is the spacing of the atoms within the slip plane and h_0 is the spacing of these planes.

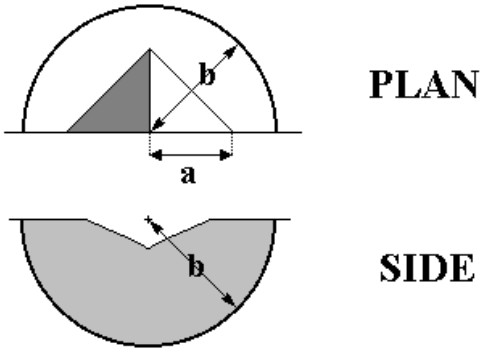

Figure 3.4: The shape and extent of the plastic zone around a Vickers elastic-plastic indentation [BR87]

3.2.2 Real Materials

The real materials possess much lower values, usually lower by order of magnitude, than the values of the theoretical strengths referred above. The possibilities to reach these theoretical values are either the preparation of defect-free, almost perfect materials or the prevention of the movement of the dislocations and the propagation of cracks. The preparation of almost perfect materials is too expensive and mostly is possible only in very small dimensions (e.g. whiskers). For the prevention of the dislocation movement and propagation of cracks a wide variety of methods has been developed. These methods are briefly listed in following:

Work hardening The strength of the materials is improved by plastic deformation. The improvement is caused by multiplication of dislocations, pile-up of the dislocations and the repulsive interaction with one another.

Accumulation of grain boundaries The yield stress of a material depends on the concentration of grain boundaries and so on the grain diameter d_g by the Hall-Petch equation:

$$\sigma_y = \sigma_i + k_y d_g^{-\frac{1}{2}}. \tag{3.6}$$

Here, $\sigma_i(T)$ and $k_y(T)$ are material constants describing the intrinsic resistance against the movement of dislocation and the efficiency of dislocation sources, respectively.

Hardening by foreign atoms The substitutional as well as interstitial atoms in solid solutions lead to increase of the yield stress. (e.g. carbon in b.c.c. iron)

Presence of the second phase The presence of a second phase in the form of a dispersion of small particles also hinders the movement of dislocations and subsequently leads to a considerable increase of the strength or the hardness. The volume fraction of the second phase and the particle size, which can be combined into the inter-particle distance d_p are decisive in this case.

3.2.3 Hardness and Bulk Modulus

Even if the *bulk modulus* K - in contrast to hardness - is defined unequivocally (as it was described above), there are several empirical and semiempirical models to relate it to the hardness. In these studies researchers are trying to predict the hardness of materials and on this basis to propose extremely hard materials.

Model of Kisly [Kis86]

The hardness of materials according to Kisly's model depends on the bond energy, the covalency of the bond and the bond length. In addition, parameters describing plastic deformation and brittle fracture are of importance (b, r_0, c_L).

$$H = \frac{E_0 a_c}{r^2}\left(B_1\frac{1}{\sqrt{r}} + B_2\frac{b}{r r_0} + B_3\frac{1}{c_L} + B_4\right) \tag{3.7}$$

E_0 is the bond energy, a_c is the degree of covalency, r is the bond length, b is the Burgers vector and c_L is the unstable crack length. B_1, B_2 and B_3 are constants.

Model of Cohen [Coh94]

It was found empirically, that for ideal, i.e. almost defect-free, isotropic systems, the hardness is proportional to K. For the bulk modulus of covalent solids, according to Cohen and Liu [Coh94], the following semiempirical dependence on the bond length r, the mean coordination number$\langle N_c\rangle$ and the ionicity of the bond Λ exists:

$$K[GPa] = \frac{\langle N_c\rangle}{4}\frac{1971 - 220\Lambda^{3.5}}{r[\text{Å}]} \tag{3.8}$$

3.2.4 Current Research Activity in Hardness Improvement

Multilayer Coatings and Superlattices Multilayer sytems with the thickness of the individual layers in the nanometer range in many cases posses improved mechanical properties (e.g. hardness and Young's modulus).

Nanocomposites Composite materials consisting of nanocrystals [SVS95, SV00] in an amorphous matrix should posses extremely high hardnesses.

Composites with Nanotubes The advantages of fibre-reinforced composites (e.g. carbon-fibre-reinforced epoxy resins) are their low density, simultaneously with high stiffness and high strength.

Acknowledgement This research was funded by the Ministry of Education, Youth and Sports of the Czech Republic, project LO1411 (NPU I) and by Czech Science Foundation project No. 15-17875S [1]

[1]Submitted: 31.7.2018; Accepted: 20.12.2019

Chapter 4

Relationships between the hardness and elastic modulus

V. Buršíková
Department of Physical Electronics, Faculty of Science, Masaryk University, Kotlářská 2, 611 37 Brno, Czech Republic

The wear process of materials exhibits rather complex character, because there are several possibilities of chemical, physical and mechanical changes at the interface (i.e. yielding, brittle failure etc.) [1]. The model proposed by Archard [4],The stochastic character of the wear process was taken into account in the well-known model proposed by Archard [4], which was taken as the basis of the majority of available models [5-9].

There are several empirical relationships between the wear rate and the mechanical properties [9] based on the ratio of the hardness (H) to the Young's modulus (E) as it is shown in Table 1 [9-11]. The most often used H to E ratios are H/E [34], H/E^2 [35] and H^3/E^2 [36]. The first ratio characterizes the resistance of the material to *elastic* deformation. Generally, high H/E values would mean, that despite it is hard to deform the material plastically, if it is done, the material will break down at once. Hard materials, which are unable to withstand plastic deformation, are usually brittle (for example, glass).The second ratio, which is expected to correlate well with abrasive and erosive wear, indicates material's ability to *resist permanent damage*. The H^3/E^2 ratio allows to estimate the material's ability to dissipate energy at *plastic* deformation during loading. This ratio is proportional to the load that defines the transition between elastic to plastic contact in a ball-on-plane system, applying the analytical solutions provided by Hertz in Contact Mechanics [12].

Parameter Physical meaning (taking into account a rigid-plastic material)

H/E Deformation relative to yielding [9]

H/E^2Resistance to the permanent damage [10]

H^3/E^2Resistance to the permanent damage [11]

$(H/E)^2$Transition on mechanical contact – elastic to plastic [9]

$H^2/2E$ Modulus of resilience [9]

Table 1 Parameters based on the hardness and elastic moduli, used as indicators of abrasion resistance and their physical meanings

The work [13] presents an equation that relates the reduced modulus with the amount of elastic recovery, h_e , considering a conical indenter:

$h_e = h - h_P = H \times \pi \times a E_r$ (1)

In Equation 1 the term Er is the reduced modulus, defined as:

$E_r = 1 - \nu_i 2 E_i + 1 - \nu^2 E$ (2)

where, E_r is the reduced modulus, E_i is the Young's modulus of conical indenter, ν_i is the Poisson's ratio of conical indenter, E is the Young's modulus of tested material, and ν is the Poisson's ratio of tested material.

The term $E/(1-\nu^2)$ can be found in ISO/FDIS 14577-1 standard [14], and it is called as 'indentation modulus', using the symbol E_{IT}. Exactly this term was used by references [5] and [6]. In this way, the mechanical properties of abrasive particle were discarded in both cases. It is notable that this aspect has not been ruled out by Stilwell and Tabor [13] in 1961.

A great difference between the Torrance's paper [5] and the Yi-Ling and Zi-Shan one [6] is with respect to the volume of wear. In the former, it was taken as directly proportional to h_2, and for the latter, related to h_{P2}, following the symbology of Figure 1. The latter can be considered as more appropriate because it takes into account the elastic effects at a worn surface, so that the final formulation provided by [6] will be presented. Thus, an equation for wear rate, Q (m^3/m), can be written as:

$Q = C\ L/H\ K_P$ (3)

where, L is the applied load, H is the hardness of worn material, C is a constant and K_P will be called here as partial wear coefficient, based on elastic effects during indentation, defined as $(1+k \times H/E)^2$, being k another constant.

In [4] the relative wear resistance was defined as

$\beta_i^* = H H_{ref} (1 + 10 H_{ref}/E_{ref})(1 + 10 H/E)$ (4)

In the literature there are also models relating the pileup formation [21] with the mechanical properties [22]. In this case, it is possible to consider that the pileup formation (h_c/h) works for static (hardness test) and kinetic cases

(scratch test), being the higher the pileup, the smaller the cutting efficiency.

In [22] an empirical relationship between the pileup (h_c/h) and the ln(E/H), based on results obtained in scratch tests can be found:

h_C/h=0.41498ln(E/H)−0.14224 (7)

Two tribological pairs were studied in [24]: glass abrading a quenched and tempered 52100 steel [25], and alumina wearing a hard metal [26].

Material H [GPa] E [GPa] E_r [GPa] H/E H/E_r

Soda-lime glass 4.07 69 53.24 0.080 0.103

Q&T steel 5.5 180* 0.023 0.076

Alumina 19.6 376.1 222.43 0.052 0.088

Hard metal (grade K) 11 480 0.023 0.049

Table 2.

Mechanical properties of selected tribological pairs. *Obs.: Q&T steel is a wire-drawing, which implies in a reduction of elastic modulus due to the work-hardening effect

Pair K_P (equation 3) K_P, (equation 4)

Glass - Q&T steel 1.41 2.66

Alumina – Hard metal 1.41 1.98

Table 3.

Partial wear coefficient values for selected tribological pairs

In addition, in reference [24] these tribological pairs were separated using the difference in the plasticity index, δH, defined in [32] (Equation 8) :

$\delta H=1-14.3(1-\nu-2\nu^2)H/E$ (8)

4. Conclusions and final remarks

The viability of the use the hardness-to-reduced modulus ratio to model the wear coefficient for abraded materials was demonstrated. Previous models were developed taking into account only the Young's modulus of worn surface, discarding the properties of abrasive material. These cases work only for pairs where the abrasive particle is harder than the abraded material and it was demonstrated that they fail when the abrasive hardness is relatively low.

In addition, other questions were discussed and they open some possibilities to carry out future research. First, the model of wear coefficient treated here involves higher requirements, because a constant is needed. This constant seems to affect more the wear coefficient of some pairs than the others, and the reason for that is not clear. Finally, an extensive work could be

made exploring the relation between cutting efficiency (abrasion factor) and H/Er ratio, computing a large variation of the applied load and the abrasive (indenter) properties. Probably, an investigation based on these aspects should supply answers to the improvement of a wear model containing the H/E_r ratio.

Acknowledgement This research was funded by the Ministry of Education, Youth and Sports of the Czech Republic, project LO1411 (NPU I) and by by Czech Science Foundation project No. 15-17875S [1]

[1]Submitted: 31.7.2018; Accepted: 20.12.2019

Part II

Indentation techniques and metrology

Chapter 5

Conventional hardness testing

V. Buršíková
Department of Physical Electronics, Faculty of Science, Masaryk University, Kotlářská 2, 611 37 Brno, Czech Republic

The hardness test is one of the most common forms of mechanical testing. A conventional test involves two steps: pressing the indenter into sample with load L and removing followed by optical measurement of the residual area A_{r} from the diagonal of the residual print.

The (residual) hardness is defined as

$$H_r = \frac{L}{A_{\mathrm{r}}} \tag{5.1}$$

The residual hardness values can be used in a number of ways to investigate the resistance of materials to permanent deformation. In conventional hardness testing the determination of the indentation size is limited by optical imaging. It is possible to form "plastic" hardness impressions in nearly every class of material, including those normally considered to be truly brittle (e.g. many ceramics and glasses). The formation of such a plastic impression indicates that under some conditions even these materials can undergo plastic deformation, albeit limited.

The Vickers microhardness indentation testing seemed to be very useful for the mechanical characterisation of thin films. It is based on the indentation of a square-based diamond pyramid with face angle $\alpha = 136^o$. Then the Vickers hardness H is obtained as a ratio of the applied load L to the area

of the resulting indentation print:

$$HV = 2\sin\left(\frac{\alpha}{2}\right)\frac{L}{u^2} \tag{5.2}$$

where u is a measured diagonal length of an indentation print.

As the geometry of the indentation is independent of its size, in principle, the microhardness is independent of the applied load. In practice there is a load dependence particularly for small loads, so called indentation-size effect ISE, caused often by the formation of pile-ups near the indentation print. The ISE has been known for a long time. However, many reports about ISE are due to artifacts [IB96]: surface layer that were not accounted, graded layers, surface hardening, etc. We can calculate the hardness (it means the hardness at higher load, where the hardness is a material constant) from empirical approach according to [NS96] or by corrections of the indentation print for pile-ups [IB96].

Recent explanations invoke the need for "geometrically necessary" dislocations at very small depths to explain the ISE effect [IB96, MN88].

One of the reasons of the ISE effect is, that the contact area A_r has not the ideal square based pyramid shape, as it is shown in Fig. 5.1.

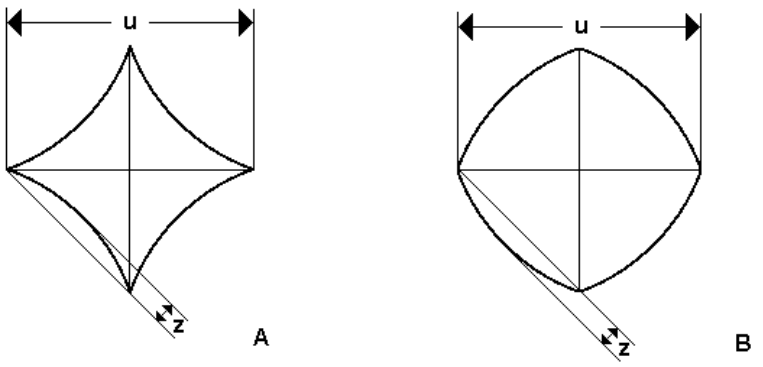

Figure 5.1: Correction of the contact area A_c for two different types of the indentation prints

The corrected hardness for indentation prints in Fig. 5.1 has the following form using the same marks as in the figure:

$$HV = 1.854\frac{L}{(u \mp z\sqrt{2})^2} \tag{5.3}$$

At small indentation prints the elastic part of the indentation work becomes a substantial part of the total indentation work. By optical imaging techniques it is not possible to determine the elastic deformation, that consequently causes overestimation of the hardness values. The solution of this problem is the depth sensing indentation test, which will be described in the following chapter.

Acknowledgement This research was funded by the Ministry of Education, Youth and Sports of the Czech Republic, project LO1411 (NPU I) and by by Czech Science Foundation project No. 15-17875S [1]

[1]Submitted: 31.7.2018; Accepted: 20.12.2019

Chapter 6

Depth Sensing Indentation Test

V. Buršíková
Department of Physical Electronics, Faculty of Science, Masaryk University, Kotlářská 2, 611 37 Brno, Czech Republic

In the past few decades, the depth sensing indentation (DSI)test [1] became widely used for characterisation of mechanical properties of various types of materials. The advantage of this technique over conventional hardness measurement method is that it enables to acquire the load dependence of the tip penetration into the tested sample. This improvement became important mainly for superhard thin film material developed , where the optical measurement of extremely small indentation imprints was very uncertain or even impossible. Moreover, the DSI method enables to evaluate the depth profile of gradient or multilayer coatings or to study the dependence of hardness on the loading rate. One of the main advantages is that the method also enables to determine the elastic modulus of the studied samples.

6.1 Indentation Load-Displacement Data

If a sharp indenter is pressed into a sample its displacement may arise from both elastic (reversible) and plastic (irreversible) deformation of the tested sample material. When the indenter is removed from the sample, elastic displacements are recovered and a residual indentation print may remain. As it was already mentioned in previous chapters, the hardness measurement was originally developed for testing metals in which the deformation is mostly

[1] Recently the method is called Instrumented Indentation Technique.

plastic (the compressive yield strength to Youngś modulus σ_y/E is small). In this case there is practically no elastic recovery under unloading, and the projected area at the maximum depth equals the residual projected area after unloading. Consenquently, the mean contact pressure at the maximum penetration depth (defined as the maximum indentation load divided by the maximum projected area A_{p} equals the maximum indentation load divided by the residual projected area A_{r} after unloading as in Fig. 6.1. The deformation under indenter is ideally plastic, the residual area of indentation print is the same as the contact area under the maximum load.

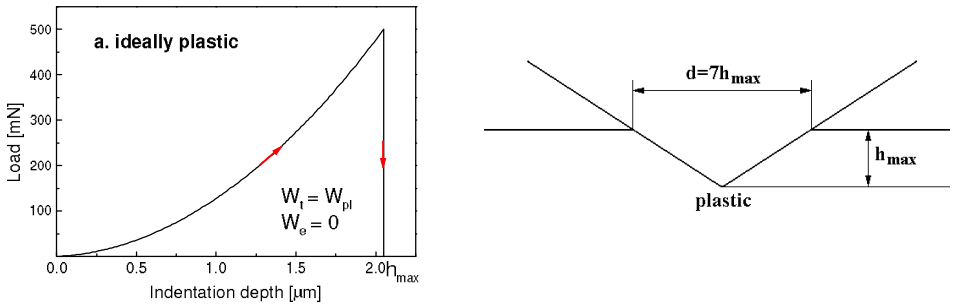

Figure 6.1: **Load-penetration curves and the schema of the residual indentation print for an ideal plastic material.** d is the diagonal length of the residual indentation print. $\mathrm{h_{max}}$ is the maximum penetration depth at the maximum load L_{max}, $\mathrm{W_t}$ is the total and $\mathrm{W_{pl}}$ is the plastic part of the indentation work.

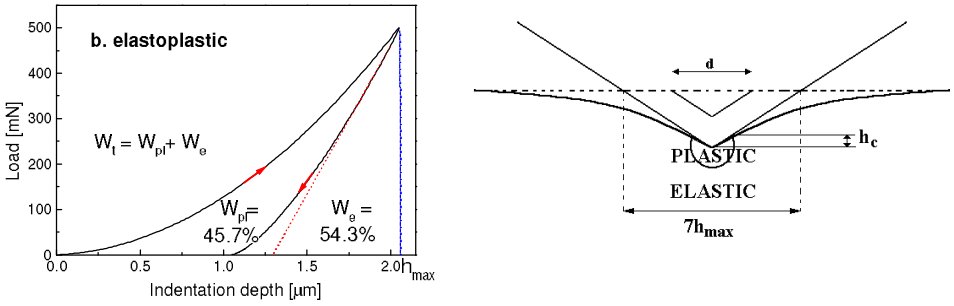

Figure 6.2: **Load-penetration curves and the scheme of the indentation print for an elastic-plastic material.** d is the diagonal length of the residual indentation print, $\mathrm{h_{max}}$ is the maximum penetration depth at the maximum load L_{max}, $\mathrm{W_e}$ is the elastic and $\mathrm{W_{pl}}$ is the plastic part of the total indentation work $\mathrm{W_t}$.

On the other hand, if the deformation is mostly elastic then a significant

portion of the contact area at maximum depth is due to the elastic deformation. Consequently, the residual projected area is smaller than the projected contact area at maximum indentation depth Fig. 6.2.

6.1.1 Elastic and plastic part of the total indentation work

The elastic and plastic part of the indentation work could be easily determined from the load - penetration hysteresis, as it is shown in Fig. 6.2. The elastic $\mathrm{W_e}$, plastic $\mathrm{W_{pl}}$ and the total indentation work $\mathrm{W_t}$ are given by the following relationships

$$\mathrm{W_t} = \int_{h=0}^{h_{\max}} L_1(h)\mathrm{d}h, \qquad \mathrm{W_e} = \int_{h_{\min}}^{h_{\max}} L_2(h)\mathrm{d}h \qquad \text{and} \qquad W_{\mathrm{pl}} = \mathrm{W_t} - \mathrm{W_e} \tag{6.1}$$

Here $L_1(h)$ and $L_2(h)$ are the loading and unloading curves. The plastic and elastic parts, $\mathrm{w_p}$l and $\mathrm{w_e}$ of the total indentation work $\mathrm{W_t}$ are then given as

$$\mathrm{w_{pl}} = \frac{\mathrm{W_{pl}}}{\mathrm{W_t}} 100\% \qquad \mathrm{w_e} = 100\% - \mathrm{w_{pl}} \tag{6.2}$$

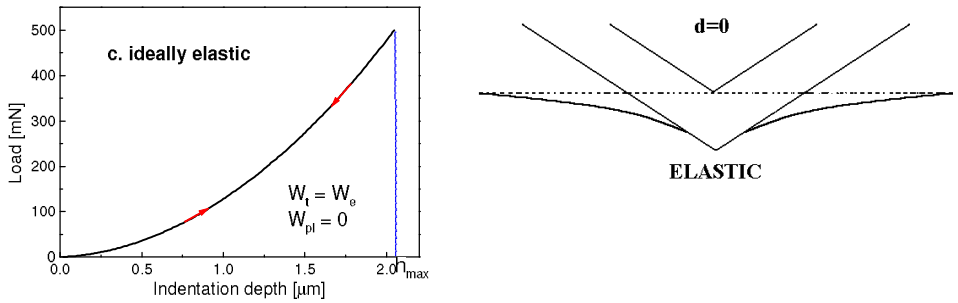

Figure 6.3: **Load-penetration curves and the scheme of the indentation print for an ideally elastic material.** $\mathrm{h_{max}}$ is the maximum penetration depth at the maximum load $L_{\max}$, $\mathrm{W_e}$ is the elastic part of the total indentation work $\mathrm{W_t}$.

Based on load - penetration curves it is possible to make a new definition of the hardness. In case of optical evaluation of the indentation print, the residual area A_{r} is measured after the indenter is removed. In the following definition A_{c} is the contact area under maximum load $L_{\max}$:

$$HM = \frac{L_{\max}}{A_{\mathrm{c}}} = \frac{L_{\max}}{26.43 h^2{}_{\max}} \tag{6.3}$$

HM is the so called Martens hardness[2] and 26.43 is a factor, which characterises the Vickers indenter geometry.

This definition can be important for materials showing a lot of elastic recovery. An example of the fully elastic indentation is shown in Fig. 6.3. The conventional hardness test would return an infinite hardness because of the zero residual area $A_\mathrm{r} = 0$. However, the depth sensing indentation test would return a finite hardness due to the non-zero indentation depth.
To summarise,

- The optical evaluation of the indentation print provides **a measure of the resistance of the material to plastic deformation.** The indentation depth in this case should be large enough to cause substantial permanent deformation. In case of a substantial elastic recovery ($\mathrm{W_e} \gg 70\%\mathrm{W_t}$) the results of optical evaluation will overestimate the hardness. **On the basis of mostly elastic deformations it is not possible to determine material parameters related to plastic deformation.**

- The depth sensing indentation test **gives an information about the resistance of the material to either elastic or plastic deformation.**

The conventional residual hardness H_r and the contact hardness HM are both useful. Moreover, in many cases (for example in the case of metals) $A_\mathrm{c} \approx A_\mathrm{r}$, and $H_\mathrm{r} \approx HM$. That does not work for materials having high strength to stiffness ratios. The hardness HM defined in 6.3 represents the average pressure underneath the indenter at maximum load. Whatever definition is used, hardness represents only a complicated average of material properties. It is important to highlight the matter of fact, that *hardness is not a fundamental physical quantity.* However, the indentation testing is a very powerful material characterisation method for describing the indentation resistance of the materials including thin films.

6.2 Data Analysis Methods

Indentation load-displacement analysis methods are powerful:
One can obtain much more information that just hardness. However, the results are very sensitive to the details of the analysis.

[2]Martens hardness is also called as universal hardness HU

6.2.1 Analysis of load-penetration curves

6.3 Doerner's and Nix's flat punch model

Doerner & Nix were the first in 1986 [?] who developed a model for calculation of hardness and elastic modulus from load-penetration dependences. They assumed, that if during unloading the change in contact area is small, the indentation could be modelled as an indentation using cylindrical flat punch. In that case the material below the indenter undergoes plastic deformation, while the material around the indenter elastic deformation only. Therefore, the material exhibits a fully elastic recovery after unloading and the unloading curve is linear. In that case the elastic unloading can be calculated according to following equation:

$$L(h) = 2ahE_{\mathrm{r}} = 2E_{\mathrm{r}}\sqrt{\frac{A}{\pi}}h \tag{6.4}$$

where a is the contact radius (radius of the cylindrical flat punch) and A is the contact area. Derivation of the load $L(h)$ according to the indentation depth h leads to the elastic unloading stiffness value:

$$S = \frac{\mathrm{d}\,L}{\mathrm{d}\,h} = 2E_{\mathrm{r}}\sqrt{\frac{A}{\pi}} \tag{6.5}$$

Plastic Hardness On the basis of Doerner & Nix approach the plastic hardness value was defined. The plastic hardness value HU_{pl} is the measure of the material resistance against plastic deformation. This value is analogical to HV value obtained on the basis of the conventional hardness measurement:

$$HU_{pl} = \frac{L_{\max}}{A_d(h_r)} = \frac{L_{\max}}{\mathrm{K}h_r^2} \quad , \quad h_r = h_{\max} - \frac{L_{\max}}{S} \tag{6.6}$$

Here h_r is the fictive depth of the remained indentation print. h_r is obtained if we extrapolate the linear part of the unloading curve, where the unloading is purely elastic.

The hardness and the reduced modulus can be then calculated from experimentally measured values of maximum load L_{max}, maximum displacement $h_{\max}$,fictive depth h_{r} and the elastic unloading stiffness S. Doerner's & Nix's method of obtaining hardness and modulus using a a flat punch approximation predicted the contact area to remain constant during unloading. This assumption is fulfilled in case of metals, where the elastic deformation work is substantially lower than the plastic deformation work (the loading-unloading behaviour is close to the situation shown in Fig. 6.1).

6.3.1 Analysis based on the metod of Oliver and Pharr

Method of Oliver and Pharr [OP92b] is the most commonly used nanoindentation analysis method. They made the following assumptions:

a) The deformation upon unloading is purely elastic

b) The compliances of the sample and of the indenter tip can be combined as springs in series

$$\frac{1}{E_{\mathrm{r}}} = \left(\frac{1-{\nu_{\mathrm{i}}}^2}{E_{\mathrm{i}}}\right) + \left(\frac{1-{\nu_{\mathrm{m}}}^2}{E_{\mathrm{m}}}\right) \tag{6.7}$$

where E_{r} is reduced modulus, E is the Young's modulus, ν is the Poisson's ratio and i and m refer to the indenter and tested material, respectively.

c) The contact can be modelled using an analytical model for contact between a rigid indenter of defined shape with a homogeneous isotropic elastic half space using

$$S = \frac{2E_{\mathrm{r}}\sqrt{A}}{\sqrt{\pi}} \tag{6.8}$$

where S is the contact stiffness and A the contact area. This relation was presented by [Sne65]. Pharr has shown that Eq 6.8 is possible to apply to tips with a wide range of shapes [OP92b, GMPB92].

Based on the relationships above, we can show, that:

- The unloading curve L_{un} follows a power law relationship

$$L_{\mathrm{un}} = \alpha(h - h_{\mathrm{r}})^m \tag{6.9}$$

h is the immediate contact depth and h_{r} is the residual depth.

- The contact depth, h_{c} (the depth along the indenter axis to which the indenter is in contact with the sample material at maximum load L_{max}), is given by

$$h_{\mathrm{c}} = h_{\mathrm{max}} - \epsilon(h_{\mathrm{max}} - h_{\mathrm{i}}) \tag{6.10}$$

where h_{max} is the maximum depth and h_{i}, the intercept depth, is the intercept of the tangent to the load-displacement data at the maximum load on unloading with the depth axis.

- The constant ϵ is a function of the shape of the indenter tip(See Table 6.1):

Indenter shape	m	ϵ
flat punch	1.0	1.0
cone	2.0	0.7268
sphere	1.5	0.75
paraboloid (small displacements)	1.5	0.75
Vickers	2	0.75

Table 6.1: Constants m (Eq. 6.9) and ϵ (Eq.6.10) as functions of the indenter shape.

6.4 Principal values obtained from DSI method

6.4.1 Hardness determination from DSI tests

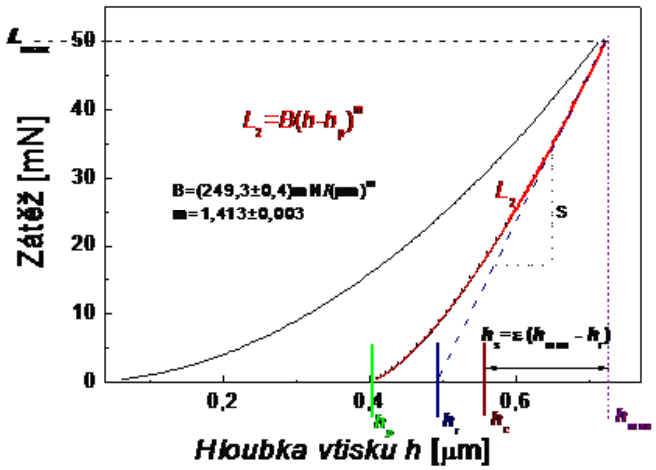

Figure 6.4: Illustration of the load-displacement curve analysis.

In Fig 6.4 there is shown an example of the load-penetration curve analysis.

$$H_{IT} = \frac{L_{\max}}{A_p(h_c)} \tag{6.11}$$

$A_p(h_c)$ is the projected area at in the Vickers hardness HV_{IT} may be obtained from H_{IT} according to the following calculation:

$$H_{IT} = \frac{9.81 \cdot L_{\max}\,[kg]}{A_d \cdot \sin(\theta/2)} = \frac{9.81}{\sin(\theta/2)} \cdot HV_{IT} \tag{6.12}$$

6.4.2 Indentation modulus (effective elastic modulus)

The total compliance C_t during an indentation experiment is the sum of the compliance of testing machine, C_m, and the contact compliance C_r given by Eq.6.7 above.

$$C_{\mathrm{t}} = C_{\mathrm{m}} + C = C_{\mathrm{m}} + \frac{\sqrt{\pi}}{2E_{\mathrm{r}}} \frac{1}{\sqrt{A_{\mathrm{p}}}} \tag{6.13}$$

If we substitute A_{p} with $\frac{L}{H}$ into 6.13 we can eliminate the influence of the unknown indenter shape (area function):

$$C_{\mathrm{t}} = C_{\mathrm{m}} + C = C_{\mathrm{m}} + \frac{\sqrt{\pi}}{2E_{\mathrm{r}}} \sqrt{\frac{H}{L}} \tag{6.14}$$

If we measure the total compliance for several different indentation loads we can fit the data $(C_{\mathrm{t}}(\frac{1}{L^{\frac{1}{2}}}))$ according to 6.14 with linear function as it is shown in Fig. ?? and calculate the machine compliance.

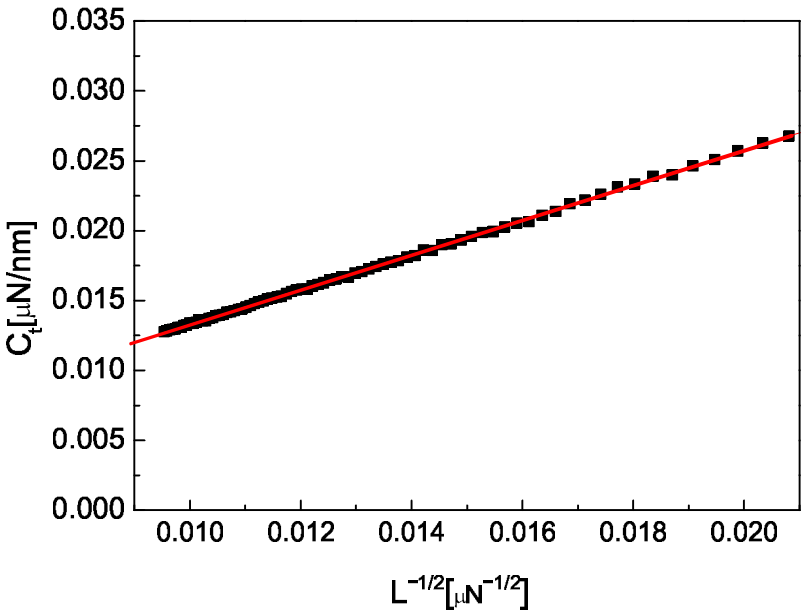

Figure 6.5: Determination of the machine compliance.

One expects the total compliance to vary linearly with the reciprocal of the square root of the contact area with intercept given by the machine compliance and slope determined by the reduced elastic modulus. We define

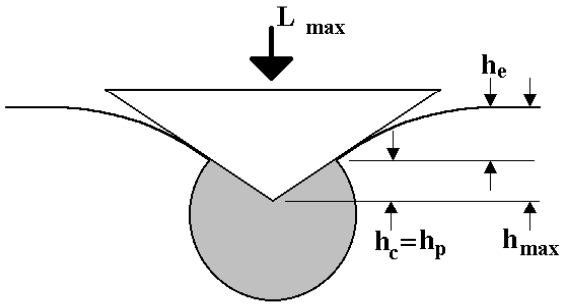

Figure 6.6: Schematic illustration of relationships between the contact depth h_c, maximum depth h_{max}, depth of the plastic deformation h_p and depth of the elastic deformation h_e. The contact depth h_c is the same as the depth of the plastic deformation h_p when $h_{max} = (h_p + h_e) > h_c = h_p$

the indentation modulus (effective elastic modulus)

$$E_{\text{eff}} = \frac{E_{\text{m}}}{1 - \nu_m^2} \tag{6.15}$$

$$E_{\text{eff}} = \frac{1}{\frac{4tan(\frac{\alpha}{2})h_i S}{\sqrt{\pi}} - \frac{1-\nu_i}{E_i}} \tag{6.16}$$

The indentation modulus (or effective elastic modulus) E_{eff} in this form is defined for a homogeneous isotropic half space. *For anisotropic materials,E_{eff} represents an average of elastic constants in all directions in the material (not just in the indentation direction!)* (Vlassak [VN93])

6.5 Principal factors affecting the depth sensing indentation measurements

6.5.1 Relationships between contact depth and the depth of elastic and plastic deformation

The size of the plastically deformed zone with respect to the contact area is different for different materials. The following figures (Figs 6.6,6.7 and 6.8) illustrate the different relations between the contact depth h_c, maximum depth h_{max}, depth of the plastic deformation h_p and depth of the elastic deformation h_e [GMPB92].

All these facts have to be taken in account in depth sensing indentation (DSI) experiments.

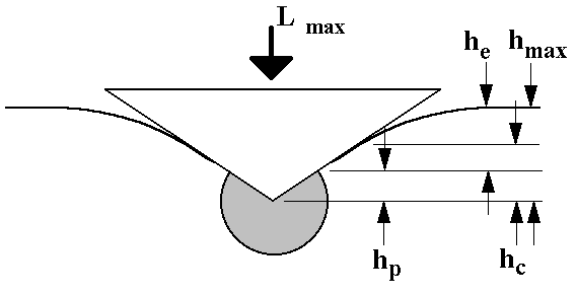

Figure 6.7: Schematic illustration of relationships between the contact depth h_c, maximum depth h_{max}, depth of the plastic deformation h_p and depth of the elastic deformation h_e, when $h_{max} = (h_p + h_e) > h_c > h_p$

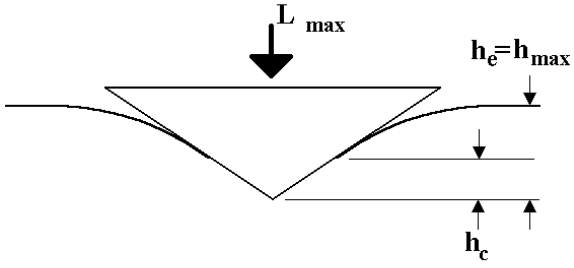

Figure 6.8: Schematic illustration of relationships between the contact depth h_c, maximum depth h_{max}, depth of the plastic deformation h_p and depth of the elastic deformation h_e when $h_e = h_{max} > h_c; h_p = 0$

6.5.2 Rate-dependence of the indentation deformation mechanism

The stress state underneath an indenter is complicated, but the (contact) hardness is just the mean pressure underneath the loaded indenter and the stress at each point underneath the indenter must scale with this value. The strain state is also complicated, but for pointed tips (pyramidal, conical) the strain at each point under the indenter due to an increment in displacement, dh, must scale with dh/h, so we define an effective strain rate

$$\dot{\epsilon} = \frac{1}{h}\frac{dh}{dt} \tag{6.17}$$

Just as in uniaxial tests of bulk materials one can then relate hardness to strain rate to determine strain rate sensitivities [MN88, BL97].

6.5.3 Time-Dependent Displacements

In quasi-static analysis, one assumes that all displacements during unloading are elastic. However, time dependent displacements arise due to thermal drift and plastic deformation.

1. Thermal drift
   (a) Room Temperature Drift: The depth sensing indentation instruments are very large compared to the displacements that they measure and are constructed of dissimilar materials. If the temperature of the instrument changes, large displacements may be recorded. (test should be done after recording smaller cyclic variations due to laboratory temperature)
   (b) Joule Heating: The depth sensing indentation instruments contain electronic devices which generate heat. If the rate of the heat generation changes, displacements may also be measured. (test should be done after recording large initial drift)
2. Time-dependent plasticity, creep
   (a) load-rate effects
   (b) indentation creep at maximum load
   (c) plastic recovery at low loads during unloading
   (d) Initially-elastic unloading can be accomplished by long hold times. However, this increases the driving force for plastic recovery at lower loads.

(e) It is difficult to minimise effects of thermal drift and time-dependent plasticity simultaneously.

(f) The ability to measure time-dependent deformation by indentation is very useful. However time dependent deformation limits the use of elastic contact models.

If the following relation are used

$$H_c = \frac{k^2}{26.43} \tag{6.18}$$

$$k = \frac{\mathrm{d}\sqrt{L}}{\mathrm{d}h} \tag{6.19}$$

the zero point determination problem is eliminated. Here k is the slope of (theoretically) linear dependence of the square root of the load on the penetration depth.

6.5.4 Surface Roughness

Data analysis models and tip shape functions assume contact between a tip of defined shape and a perfectly smooth elastic half space. Surface roughness can reduce the actual contact area at given indentation depth leading to reduced hardness values. Roughness also leads to uncertainty in location of sample "surface" and thus in absolute values of depth.
These effects are very sensitive to roughness amplitude and wavelength. The indentation depth must be enough "large" relative to roughness:

$$h_{crit} > 20R_a, \qquad or \qquad h_{crit} > 2R_{max} \tag{6.20}$$

.

where R_a is the mean microroughness value and R_{max} is the maximum microroughness.

6.6 Effect of "Pile-up"

As it was mentioned above, materials with low strength/stiffness ratio may "pile up" during indentation, resulting a greater contact area than expected by the indentation theory. This leads to overestimation of the contact area values by up to 50% [Bol]. The overestimation is due to the fact that the theory is based on elastic contact analysis, which is quite unsuitable for a pile-up description, because during elastic deformation only sink-ins occur.

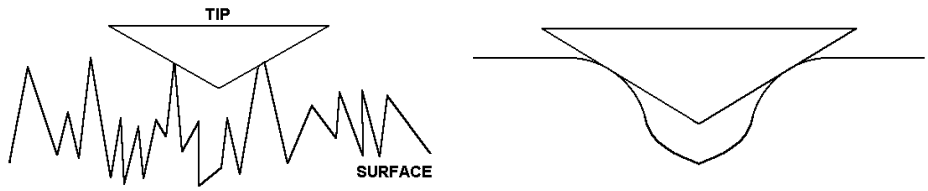

Figure 6.9: Two examples of the extreme influence of the surface roughness on the hardness measurement

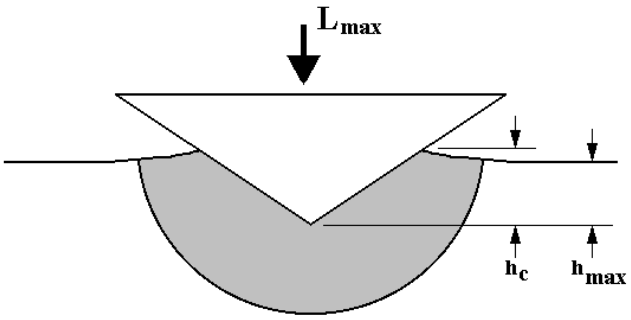

Figure 6.10: Schematic illustration of "pile up"s during indentation

Pile-up is generally affected by the ratio of effective modulus to the yield stress, E_{eff}/σ_y and the work-hardening behavior. It is lowest for a low E_{eff}/σ_y ratio and a high capacity for work hardening. This capacity inhibits pile-ups (materials at the surface close to the intender harden during deformation and constrain upward flow of material to the surface). A criterion for easy determination whether pile-up will occur is the h_f/h_{max} ratio which is $0 < h_f/h_{max} < 1$. (h_f is the final indentation depth, h_{max} is the maximum indentation depth). The low limit represents fully elastic behavior, the upper limit fully plastic deformation. In case of $h_f/h_{max} < 0.7$ very little or no pile-up is observed no matter what the work-hardening capacity of the material. If pile-up is suspected, indentations should be imaged. For example 6.11 for Vickers intenders, indentations with a large amount of pile-up can be identified by the distinct bowing out at the edges of contact impression. In case of significant pile-ups, the real contact area should be measured for example by atomic force microscopy (AFM).

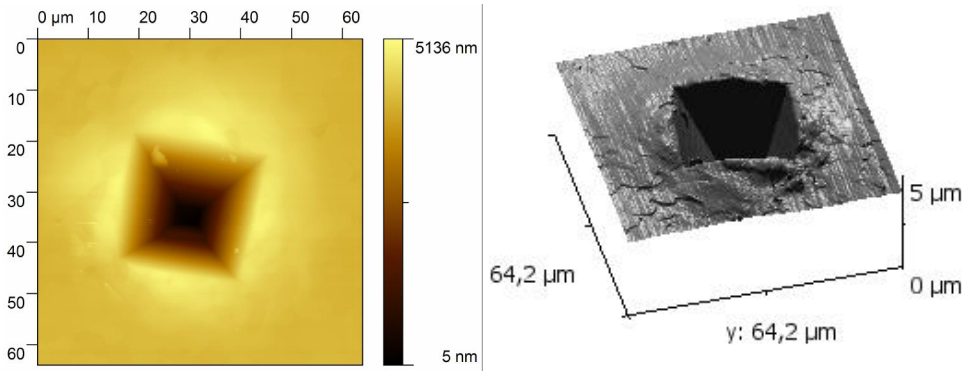

Figure 6.11: Pile-ups measured using atomic force microscopy technique after indentation of aluminium sample with maximum indentation load of 1N.

6.7 Analysis of load-penetration curves

The analysis of the nanoindentation data is focused mostly on the unloading part of the load-penetration data. However, the loading curve may contain a lot of useful information too. Based on the results of their FEM calculations Giannakopoulos and Larsson [A.E94], [PLLV96] suggested the following expression for the loading part of the indentation load-penetration curve:

$$L = \frac{B}{\beta}\sigma_y \left(1 + \frac{\sigma_u}{\sigma_y}\right) (\tan\theta)^{-2} \left[1 + \ln\left(\frac{E\tan\theta}{3\sigma_y}\right)\right] h^2. \tag{6.21}$$

Here L is the applied load, h is the total penetration depth during loading, B is a numerical constant from the FEM calculation, E is the Young's modulus. σ_y is the compressive yield strength and σ_u is the ultimate yield strength of the material.
For Vickers indentation $B = 1.19$ and $\theta = 22^o$. The surface displacement factor β is given by

$$\beta = \frac{24.5H}{C} \tag{6.22}$$

where

$$C = \frac{L}{h^2}$$

is a curve-fitting constant for the loading curve.
If the material shows

- sinking-in during indentation, then the surface displacement factor $\beta > 1$;

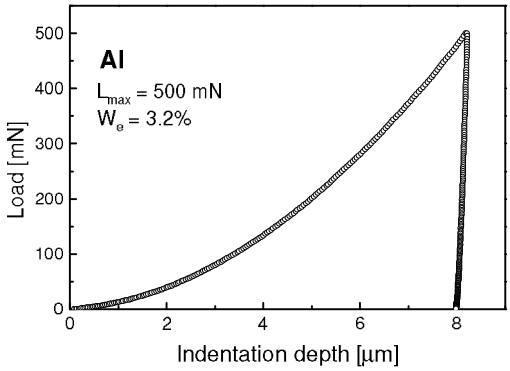

Figure 6.12: Fitting of the load - penetration curve of aluminium sample using Eq. 6.21. The curve fitting constant $C = (7.67 \pm 0.02)\ GPa$ and the surface displacement factor $\beta = 0.92$.

- pile-up,then the surface displacement factor $\beta < 1$ and
- no displacement outside the contact, then $\beta = 1$.

The next figures show typical Vickers load-penetration curves for three different materials. The computed loading curves calculated according to Eq. 6.21 are also plotted in these figures.

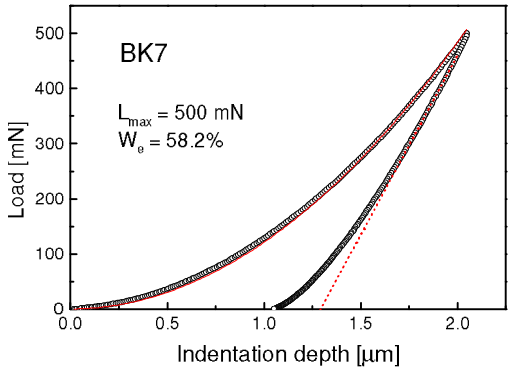

Figure 6.13: Fitting of the load - penetration curve of borosilicate glass sample (BK7, Schott AG; BK7 is used as reference material for recording hardness measurements) using Eq. 6.21.The curve fitting constant $C = (120.8 \pm 0.3)\ GPa$ and the surface displacement factor $\beta = 2.09$.

Acknowledgement This research was funded by the Ministry of Education, Youth and Sports of the Czech Republic, project LO1411 (NPU I) and by by Czech Science Foundation project No. 15-17875S. [3]

[3]Submitted: 31.7.2018; Accepted: 20.12.2019

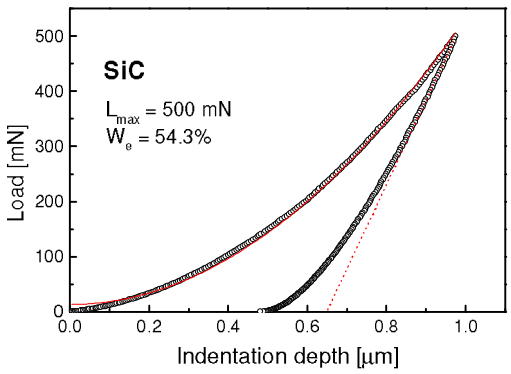

Figure 6.14: Fitting of the load - penetration curve of silicon carbide sample using Eq. 6.21.The curve fitting constant $C = 543 \pm 2$ and the surface displacement factor $\beta = 1.74$.

Chapter 7

Nanodynamic Analysis

V. Buršíková and R. Václavík
Department of Physical Electronics, Faculty of Science, Masaryk University, Kotlářská 2, 611 37 Brno, Czech Republic

7.1 NanoDMA in General

In nanoDMA, in contrast to quasistatic indentation test, a periodically varied force $F_o \sin(\omega t)$ is superimposed on the quasistatic load at frequencies in the range from 0.1 to 30 Hz.

The analysis of the dynamic test is derived from the classical equation for a single degree of freedom harmonic oscillator as given in 7.1,

$$F_o \sin(\omega t) = mx(t)'' + Cx(t)' + kx(t) \tag{7.1}$$

where F_o is the magnitude of the sinusoidal force, ω is the angular frequency of the applied force, m is the mass, C is the effective damping coefficient and k is the effective stiffness of the sample-typ system. (The term *effective*)is used to emphasize that these values describe the entire tip-sample configuration.

The solution of the differential equation 7.1 is the following periodic displacement

$$X(t) = X_o \exp[\mathrm{i}(\omega \mathrm{t} - \phi)]. \tag{7.2}$$

Inserting formula 7.2 into formula 7.1 the amplitude of the tip displacement is X_o is obtained:

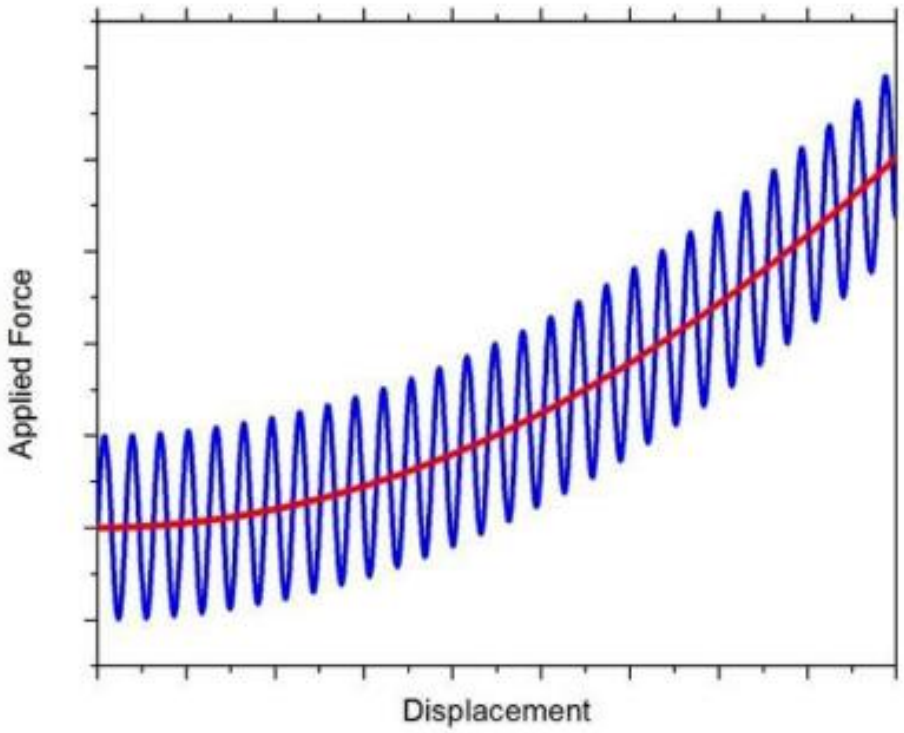

Figure 7.1: Sinusoidal oscillation force superimposed on quasistatic force

$$X_o = \frac{F_o \exp(\mathrm{i}\phi)}{k - m\omega^2 + i\omega C} \tag{7.3}$$

$$X_o = \frac{F_o}{\sqrt{(k - m\omega^2)^2 + ((C_i + C_s)\omega)^2}}. \tag{7.4}$$

The phase shift ϕ between the applied force and the resulting displacement is given in 7.5

$$\phi = \tan^{-1}\frac{\omega C}{k - m\omega^2} \longrightarrow \phi = \tan^{-1}\frac{(C_i + C_s)\omega}{k - m\omega^2}, \tag{7.5}$$

where the total spring stiffness, k, and the total damping coefficient consist of two parts. In order to decouple the indenter and the sample contribution a Kelvin-Voigt mechanical equivalents model is used.

The indenter and the sample is described by a viscous damper and a purely elastic spring, which are connected in parallel

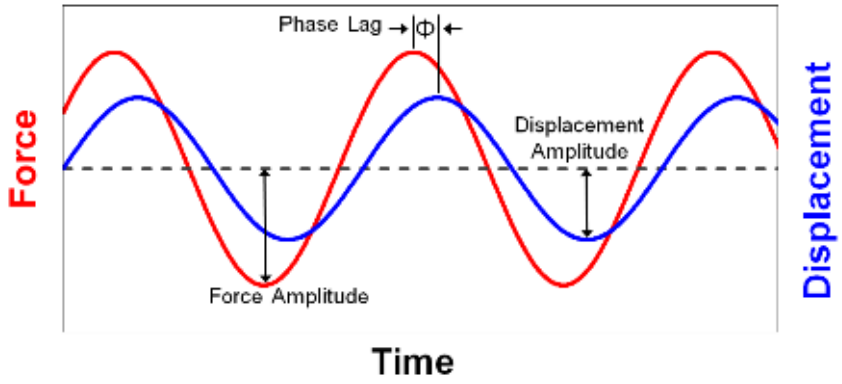

Figure 7.2: Response of the tip displacement to the dynamic force in case of viscoelastic materials

$$k = k_s + k_i \tag{7.6}$$

$$C = C_s + C_i \tag{7.7}$$

The subscripts in equations 7.6, 7.7 and 7.8, i and s refer for indenter and sample, respectively. The characteristic dynamic parameters of the system (the mass m, damping coefficient C_i, and stiffness k_i) are determined from the system calibration, X_o and ϕ are obtained from the measurement. The unknown variables k_s and C_s may be calculated from equations 7.2 and 7.3 assuming linear viscoelastic response. The stiffness k_s and damping C_s can be used to calculate the storage modulus E', loss modulus E'', loss factor $\tan\delta$, and storage K' and loss stiffness K''. The contact stiffness is the load divided by the displacement.

$$K^* = K' + iK'' = \frac{F\exp(\mathrm{i}\omega t)}{X} = \frac{F}{X_0}\exp(\mathrm{i}\phi) = \mathrm{K} - \mathrm{m}\omega^2 + \mathrm{i}\omega\mathrm{C}$$
The real and imaginary parts corresponds to storage and loss stiffness
(7.8)

Using the measured parameters, the stiffness and the damping coefficient can be calculated

$$|K^*| = \sqrt{(K - m\omega^2)^2 + \omega^2 C^2} = \frac{F}{X_0} \tag{7.9}$$

$$K' = |K^*|\cos(\phi) = K - m\omega^2; \quad K'' = |K^*|\sin(\phi) = \omega C \tag{7.10}$$

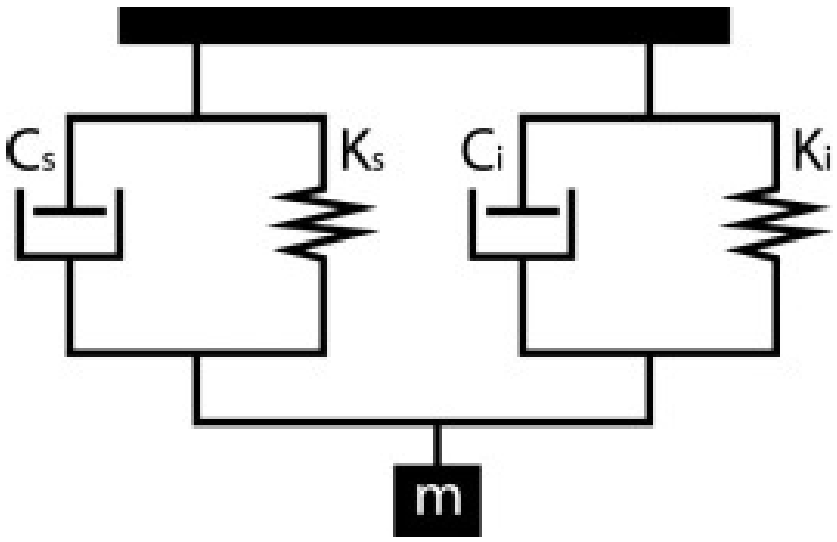

Figure 7.3: Kelvin-Voigt mechanical equivalent model used to describe the contact stiffness and damping of the sample-tip system

$$k_s = |K^*|\cos(\phi) + m\omega^2; \quad C_s = \frac{|K^*|\sin(\phi)}{\omega} \tag{7.11}$$

$$E' = \frac{k_s\sqrt{\pi}}{2\sqrt{A_c}}; \quad E'' = \frac{\omega C_s\sqrt{\pi}}{2\sqrt{A_c}} \tag{7.12}$$

Equation 7.13 shows the relationship between complex modulus (denoted as E^*), storage modulus (denoted as E'), and loss modulus (denoted as E''), where i is the imaginary unit (A_c is the projected contact area between the tip and the sample).

$$E^* = E' + iE'' \tag{7.13}$$

The storage modulus E' is the measure of the energy stored and recovered during the loading period and the loss modulus E'' is the measure of the energy dissipated in the studied material during the loading period. The loss factor $\tan\phi$ is the measure of viscoelastic behavior of materials [?]. Relatively low $\tan\phi$ values indicate a predominantly elastic behaviour (low damping) of the material, high values of $\tan\phi$ indicate low damping of the studied material.

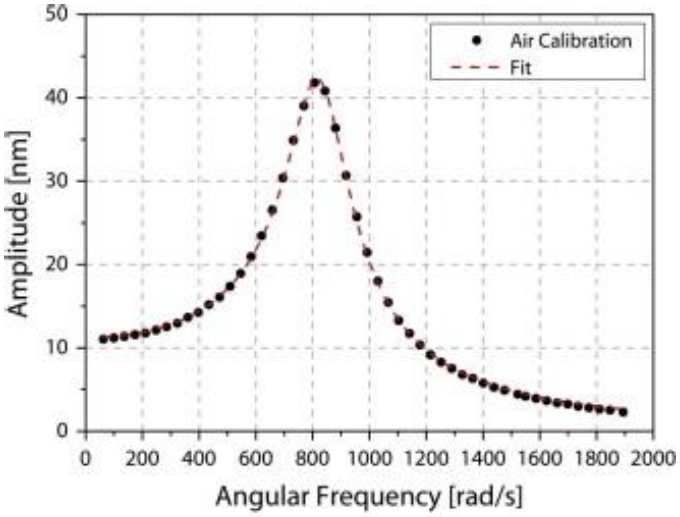

Figure 7.4: Example of the calibration procedure

7.2 Summary

Using the nanoDMA technique, a wide variety of tests can be performed. One of them is the frequency sweep (1 – 300 Hz) method, which show how the mechanical properties change with applied frequency. Load sweeps can also be performed which consist of a series of measurements performed at increasing quasi-static loads and a constant frequency to show the mechanical properties as a function of depth into the sample.

The nanoDMA technique is very useful for relatively soft or viscoelastic samples such as polymers or biological materials.

Acknowledgement This research was funded by the Ministry of Education, Youth and Sports of the Czech Republic, project LO1411 (NPU I) and by by Czech Science Foundation project No. 15-17875S [1]

[1]Submitted: 31.10.2019; Accepted: 20.12.2019

Chapter 8

Metrological traceability

Anna Charvátová Campbell[1], Petr Klapetek[1,2],
[1]*Czech Metrology Institute, Okružní 31, 638 00, Brno, Czech Republic*
[2]*Central European Institute of Technology, Brno University of Technology, Purkyňova 123, 612 00 Brno, Czech Republic*

Metrological traceability is an important concept in assuring the quality of measurement results. It plays a key role for any comparisons, especially between different methods or laboratories. Technically it is defined according to International vocabulary of metrology (VIM) [VIM12] as "property of a measurement result whereby the result can be related to a reference through a documented unbroken chain of calibrations, each contributing to the measurement uncertainty ". In this context the "reference" can be a definition of a measurement unit through its practical realization, or a measurement procedure including the measurement unit, or a measurement standard. Thus metrological traceability requires a calibration hierarchy, with international standards or national standards at its top. These are calibrated by inter-laboratory comparisons to assure their values and accuracy. For measurements with more than one input quantity, each of the input quantity values should itself be metrologically traceable. A detailed review on the traceability of hardness measurements can be found in [GHL10] and in [HPK+14]. Direct calibration includes

- calibration of the applied force
- calibration of the displacement measurement
- calibration of the machine compliance
- calibration of the indenter area function.

For measurement devices two types of calibrations are commonly used: direct and indirect. Direct calibration consists of a direct comparison of the output with the indication of the corresponding reference etalon. Thus we obtain the calibration of a whole range of values. However, depending on the design of the device the sensors may not be easily accessible and the procedure may be cumbersome or even impossible. Indirect verification uses reference samples with a certified property, e.g. hardness or stiffness. The verification consist in a simple measurements according to a prescribed protocol. The disadvantage is that, the calibration holds only for the value of the reference sample. Extrapolation to other values may not be justified. In order to cover a desired range of values, several reference samples may be needed. Indirect verification should be performed regularly. Direct verification should be performed at regular intervals, e.g. the ISO norm 14577 [ISO15b] recommends a 3 year interval for instrumented indentation devices, or if indirect verification fails.

8.1 Calibration of the depth sensor

Several well established methods can be used for traceable measurements of the displacement, e.g. laser interference method, inductive method, capacitive method and piezo-translator method. For a desired accuracy of modulus and hardness around 5 % an accuracy of the calibration below 0.5 % necessary [PKNS05]. For this purpose laser interferometry is especially well suited. As all direct methods their disadvantage is the fairly high cost of equipment and the difficulties of adapting them for this particular use. For a quick check the imprints on a suitable sample can be measured by a different method e.g. atomic force microscopy. If the same reference sample is used, the data also provide information about the aging of the instrument or can be used for comparison with other instruments. Two examples are explained in more detail below.

Differential interferometer A differential interferometer can be used to study directly the movement of the indenter tip. A piezo-translator monitored by an interferometer is used as an indentation sample. The indenter performs an indentation with a long holding period. During this time the voltage on the piezo-translator can be changed which results in a movement of the sample surface. The feedback loop in the nanoindenter moves the tip accordingly and records the movement as a change in the indentation depth while the interferometer measures the position of the piezo-translator. The data from the nanoindenter and the interferometer we can find a calibration curve, a typical such curve is shown in Fig. 8.1. The laser wavelength is traceable to the SI meter. The effectivity of this method depends on the

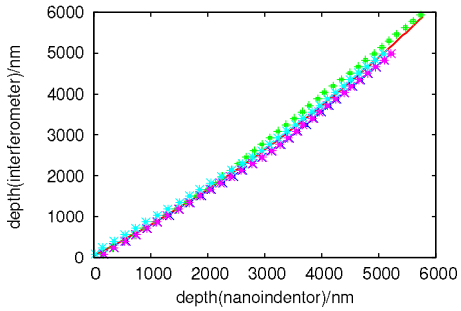

Figure 8.1: Example calibration data for depth sensor and the resulting fit.

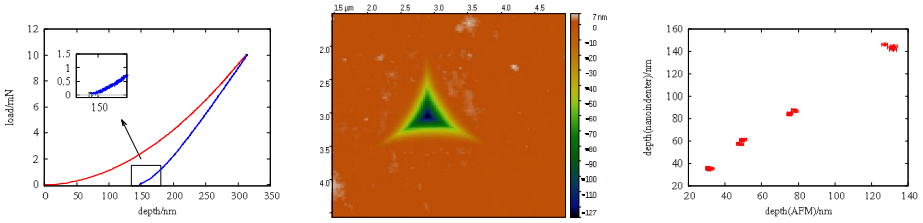

Figure 8.2: Left: The determination of the residual depth from the unloading curve on fused silica. A detail of the very last contact of tip and sample is shown in the inset. The position of the residual depth is indicated by the green box. Middle: AFM image of the corresponding indent. Right: Depth as determined by AFM and from indentation.

design of the nanoindenter: the feedback loop of the nanoindenter may impose limits on the movement of the piezo-translator and nonlinearities of the depth sensor are difficult to incorporate.

AFM A very simple calibration method is the measurement of indents by AFM. A set of indentations is performed for different loads. AFM measurements can be made traceable using appropriate step height standards. The two main sources of uncertainties are the roughness of the sample which increases the uncertainty of the AFM measurement and the exact determination of the residual depth of the nanoindentation. The determination of the residual depth from the unloading curve may be difficult due to drift. The very last portion of the unloading curve should be fitted by a suitable function. For more elastic samples the determination of the residual depth from the unloading curve may have an uncertainty of 1–2 nm, see also Fig. ??. In order to minimize it, it may be necessary to modify the unloading protocol: e.g. increase the acquisition rate, decrease unloading rate or include a hold period at very low load.

8.2 Calibration of the load sensor

Traceable force sensors and force transfer standards have been studied thoroughly in the past years [PKNS05, NMFB09, LSK+07, SRS+10, KPBJ12, KP10]. Special devices can measure forces with a resolution of tens of piconewtons [NMFB09] and uncertainties can go below 1 nN. However, these are in general dedicated devices which are not accessible for ordinary calibrations of instruments. In order to transfer the force standard artefacts are necessary; the most popular ones are mass artifacts, stiffness references and force cells. Force cells are usually micro-mechanical system (MEMS) devices with deflection measurement on board and small physical dimensions so that they can be used in instruments like nanoindentors and AFMs. A variety of piezeresistive cantilevers have been produced, they are available also commercially.

Stiffness references are passive artifacts with a calibrated stiffness along a given direction. They are probably the simplest and the most available option for indenter calibration. The calibrated stiffness allows to transfer the force if both the standard and the target instrument (in our case nanoindentor) have a traceable displacement measuring system. The involvement of the length metrology necessarily increases the overall uncertainty but the simplicity of the method and the low production costs have made this method very popular. Cantilevers used in AFM or similar ones are very well suited for this purpose due to their size, stiffness and mainly low cost. These are first calibrated on a high quality mass comparator and then placed in the nanoindentation instrument.

An example of a calibration of the force sensor of a nanoindentation instrument using an AFM cantilever as a transfer standard and a mass comparator is described in [CVZK11] The setup is shown schematically in Fig. ??. The cantilever is attached to a piezoelectric transducer which has been calibrated by an interferometer. It is then pushed against a flat sample lying on a mass comparator which measured the corresponding force. A laser beam and position sensitive detector were used to to measure the deflection of the cantilever. Additionally, not shown in the scheme, the position of the comparator was monitored by an interferometer. Processing the distance-force data the stiffness of the cantilever can be obtained.

After that the cantilever is placed under the tip of the nanoindenter. The precision of the positioning system is around 1 μm so that it is possible to position to perform loading experiments at defined positions along the cantilever, as shown in Fig. 8.4. If the position is too close to the fixed end, the plastic deformation is too large and the response is not linear. On the other hand if the position is too far out the response is nonlinear or the displacements may exceed the range of the instrument.

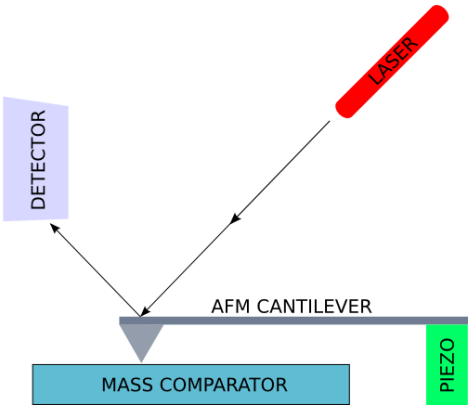

Figure 8.3: Schematic setup for the calibration of an AFM cantilever using a mass comparator.

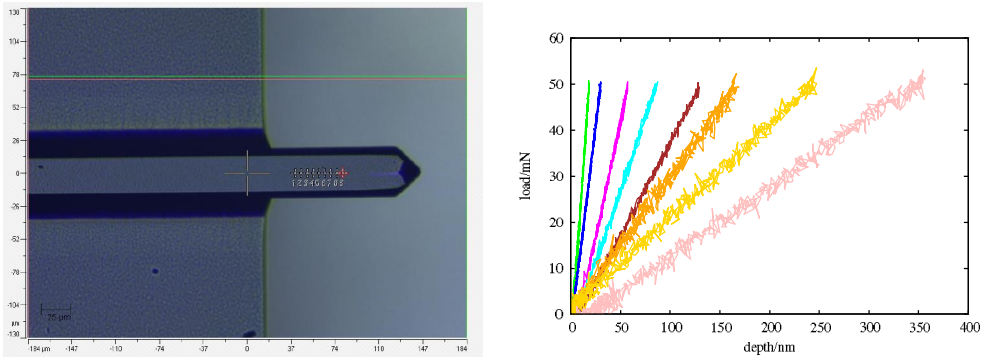

Figure 8.4: Picture of the positions where the loading measurements are performed (left) and the corresponding loading curves (right).

Figure 8.5: A cantilever of length L and thickness t is loaded at a distance y from the clamped end with load F, the corresponding deflection is Δz.

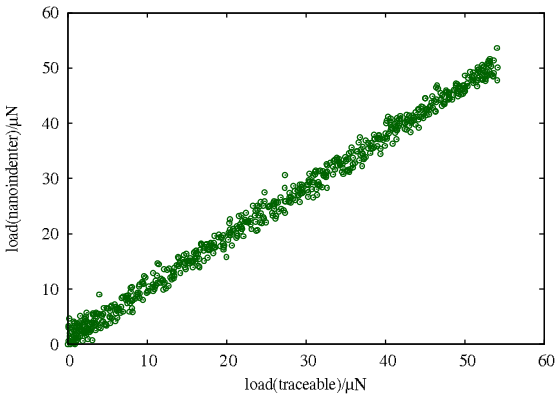

Figure 8.6: Calibration curve obtained using an AFM cantilever as transfer standard.

The stiffness of a cantilever, i.e. the ratio of load over deflection, which is loaded at a distance y from the clamped end is

$$c = \frac{F}{\Delta z} = k\left(\frac{L}{y}\right)^3 \tag{8.1}$$

where L is the length and k is the stiffness if it is loaded at the free end, see Fig. 8.5.

Thus for each loading curve we get a relation between the load indicated by the instrument and the load which is calculated from Eq. 8.1 using the calibrated value of the displacement and the stiffness calibrated on the mass comparator. An example of such a calibration curve is shown in Fig. 8.6 for a very low load range. It can be further analyzed and, if desired, fitted by a suitable function.

8.3 Calibration of the tip shape

Tip shape calibration is a routine measurement which should be performed on a regular basis. How often it should be performed depends on the use and the samples it was used on. Especially for measurements with very sharp

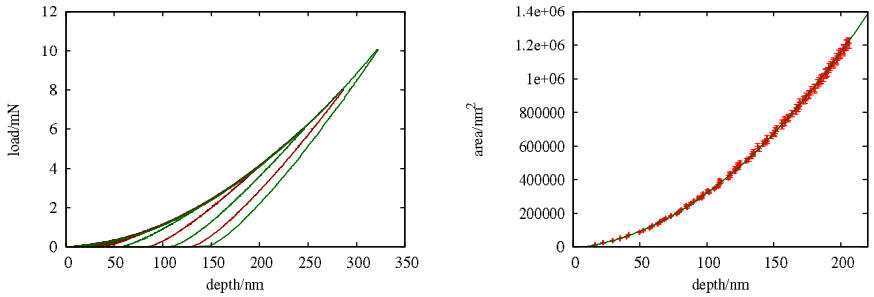

Figure 8.7: Set of loading curves on fused silica (left). Resulting area function, a polynomial up to power 1/8 was used.

tips on very hard samples it may be necessary to calibrate the area function as often as every week or even less. The two most common procedures are indentations on a reference sample [OP92a] and the direct measurement by atomic force microscopy (AFM) [HJW+00, GAS05, BSP+10]. The first method uses a reference sample, glasses such as fused silica and BK7 are very popular, and perform a large number of indents. The reference samples have a calibrated elastic modulus, so that by using the Oliver-Pharr method the area for each contact depth can be computed. The data are then usually fitted by a polynomial. Oliver and Pharr suggested [OP92a] the form

$$A = p_2 h_c^2 + p_1 h_c^1 + p_{1/2} h_c^{1/2} + p_{1/4} h_c^{1/4} + p_{1/8} h_c^{1/8} + \dots .$$

Most instruments have a routine implemented for this purpose, so that the determination of the area function is very comfortable for the user. It is necessary to choose a reference sample with low pile-up since the Oliver-Pharr method cannot treat pile-up and the area is not correctly computed. Fused silica and BK7 are very popular choices. In order to make this method traceable a traceable reference sample is required. The order of the polynomial function should be chosen carefully. For higher orders the quality of the fit inside the calibration interval is very good but rapidly decreases outside. An illustrative example is in Fig. 8.7.

On the other hand direct measurement by AFM can provide data of the tip shape per se. Traceability in AFM is a well-established concept and uncertainties as well as measurement artifacts are well-known. In general, area values for higher depths can be obtained by this method, which are difficult to obtain using nanoindentation. The disadvantage is the time needed and the risk of damage to the tip during manipulation. The data processing is tedious, the data must be corrected for the calibration of sensors, convolution with the AFM tip, alignment of the indenter tip and other possible sources of bias, depending on the instrument. The area is then determined by pixel counting. A typical AFM image of a Berkovich tip and its 3D reconstruction are shown in Fig. 8.8.

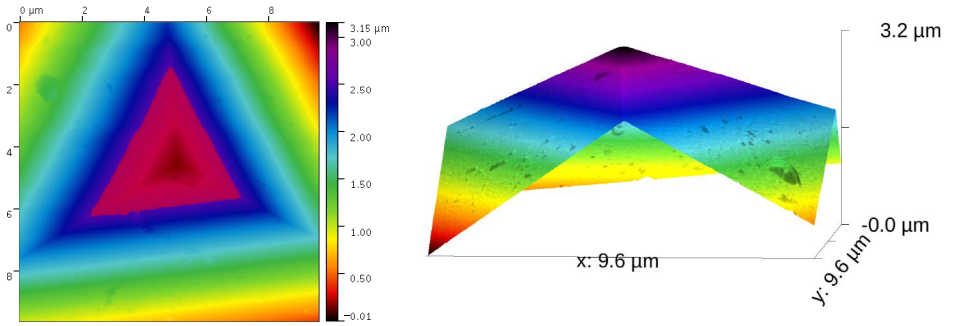

Figure 8.8: AFM image of a typical Berkovich tip with a mask showing the area corresponding to a depth of 630 nm (left) and its 3D reconstruction (right).

A comparison of the two methods for a sphero-conical tip can be found in [CĹKBss].

8.4 Calibration of the machine compliance

The calibration of the machine compliance usually follows the same procedure as the calibration of the tip shape using nanoindentation described in [OP92a]. In this case, it is recommended to use a sample with a high ratio of $E_{IT}/\sqrt{H_{IT}}$, e.g. tungsten. It can also be performed simultaneously with the tip shape calibration and both are often implemented together. For some instruments the uncorrected data may not be accessible to the user.

8.5 Uncertainties

The accuracy of the measurement result is a crucial parameter of the whole measurement process. The uncertainty is a non-negative parameter characterizing the dispersion of the quantity values being attributed to a measurand, based on the information used [VIM12]. The Guide to the expression of uncertainty in measurement [ISO08b] gives a detailed description of the evaluation of uncertainties. In general many effects contribute to the total uncertainty. They can be divided into two groups based on the type of evaluation: Type A and Type B evaluation. Type A evaluation consists of statistical analysis of the measured values, Type B evaluation includes any other means. Other means can include information from calibration certificates, information about drift, information obtained from the accuracy class of the instrument, limits based on personal experience and others. The classification in Type A and Type B is only for convenience of discussion and refers only to the mean of evaluation. It does not indicate any difference in the nature of the components. Both types are based on probability distributions function (PDF) and are both quantified by variances or standard deviations. For Type A the probability distribution function is derived from the observed frequency distribution; for Type B it is assumed based on other knowledge. All contributions should be combined and listed in an uncertainty budget. The uncertainty budget provides a comparison of the different contributions and can be used for strategic decisions concerning the improvement of the measurement accuracy.

Usually the measurand Y is not measured directly but is determined from other quantities $X_1, \ldots, X_N$ as

$$Y = f(X_1, \ldots, X_N), \tag{8.2}$$

where f may be an equation or a whole algorithm. The estimate of the measurand Y, denoted by y, is obtained from the input estimates $x_1, \ldots, x_N$ as

$$y = f(x_1, \ldots, x_N). \tag{8.3}$$

The combined standard uncertainty of y, denoted $u_c(y)$, is given by a combination of the variances of the standard uncertainties of the input estimates, called the law of propagation of uncertainty

$$u_c(y) = \sum_{i=1}^{N} \sum_{j=1}^{N} \frac{\partial f}{\partial x_i} \frac{\partial f}{\partial x_j} u(x_i, x_j), \tag{8.4}$$

where $u(x_i, x_j)$ is the estimated covariance associated with x_i and x_j. Since the diagonal elements of the covariance are the variances of the estimates

$u(x_i, x_i) = u(x_i)^2$, this can be written also as

$$u_c(y) = \sum_{i=1}^{N} \left(\frac{\partial f}{\partial x_i} \right)^2 u(x_i)^2 + 2 \sum_{i=1}^{N-1} \sum_{j=i+1}^{N} \frac{\partial f}{\partial x_i} \frac{\partial f}{\partial x_j} u(x_i, x_j); \tag{8.5}$$

the second term vanishes for uncorrelated variables. The partial derivatives are called sensitivity coefficients and describe how the output changes with varying input. For highly nonlinear models, the use of higher derivatives can be necessary, see [ISO08b].

Type A evaluation:
If repeated observations $x_1, \ldots, x_n$ are available for a quantity which varies randomly the mean or arithmetic average is a common way to estimate the expectation

$$\bar{x} = \frac{1}{n} \sum_{i=1}^{n} x_i. \tag{8.6}$$

The uncertainty can be estimated by the sample standard deviation of the mean $u(x) = s(\bar{X})$ where

$$s^2(\bar{X}) = \frac{1}{n(n-1)} \sum_{i=1}^{n} (x_i - \bar{x})^2. \tag{8.7}$$

The covariance associated with two variables X and Z for which n independent pairs of simultaneous observations are available can be estimated as

$$u(x, z) = \frac{1}{n(n-1)} \sum_{i=1}^{n} (x_i - \bar{x})(z_i - \bar{z}). \tag{8.8}$$

Type B evaluation:
If there are no repeated observations available, the uncertainty must be estimated based on all information obtainable. Probability distribution functions must be constructed based on previous measurements, long term experience, certificates etc. One of the most common cases is the situation when the only knowledge available is an interval $[a_-, a_+]$ within which the value X should lie. In this case one can assume a uniform distribution, which states that all values in the interval have an equal probability and all values outside have zero probability. For such a probability distribution the expectation value of X and the associated variance are given as

$$x = \frac{1}{2}(a_- + a_+) \tag{8.9}$$

$$u^2(x) = \frac{1}{12}(a_+ - a_-)^2. \tag{8.10}$$

A more general approach is the propagation of distributions. This approach uses the information on the model to propagate the PDFs of the input

variables X_i to obtain a PDF for the measurand Y. This PDF is then used to obtain the estimate of the output, its uncertainty and possibly other information. Thus the distinction between Type A and Type B uncertainties vanishes and all input variables are treated equally. The propagation can be done either analytically, by Taylor series approximations or numerically. Analytical solutions are possible only for very simple cases. First order Taylor series lead to the law of propagation of uncertainty. The numerical propagation using Monte Carlo methods is described in two supplements to the GUM [ISO08a, ISO11]. The requirements for the Monte Carlo method are less restrictive than for the law of propagation of uncertainty, so it can be used also in cases when the law of propagation does not hold. The procedure is the following:

1. select the number M of Monte Carlo trials
2. generate M vectors $X_1, \ldots, X_N$ according to the PDFs
3. for each such vector evaluate Y and assemble a PDF for Y
4. use the PDF to calculate the estimate y and the standard uncertainty $u(y)$

The number of trials determines the quality of the results. For a desired numerical tolerance it depends on the model which is calculated and cannot be guessed a priori. Adaptive procedures are available [ISO08a]. For simple models an initial guess $M = 10^4$ is reasonable, also as a starting point for adaptive procedures. The advantages of the Monte Carlo method are the simple treatment of even highly complex models and improvement in the determination of both estimate and uncertainty, especially for non-linear models and distributions other than Gaussian or Student. It may be however more time consuming since the computation time grows linearly with the number of trials M.

8.6 Uncertainties in instrumented indentation measurements

The ISO standard [ISO15a] recommends two approaches to uncertainty estimation. The first is based on a comparison with respect to a reference block and assumes that the uncertainties are the same for indentations on a test sample as for the reference block. The second approach takes into account all identified contributions to the uncertainty. The most significant contributions are:

1. **Noise of the load and depth sensor:** The noise of the sensors is one of the most obvious sources of uncertainty. The technical specifications provided by the manufacturer may be used but estimates based on long term experience are preferable. The noise can be estimated e.g. from periods where the tip is not in contact with the sample or for suitable hold periods. For the Oliver-Pharr model and similar models, the noise of the sensors enters the formulae for hardness and modulus explicitly as well as implicitly in the fitting procedure. Different treatments of fitting a linear function are compared in [MP13], however not everything can be translated to nonlinear functions such as the Oliver-Pharr power law function.

2. **Determination of zero point:** The determination of the exact point of contact between tip and surface is not trivial and can easily lead to significant uncertainties. It can be determined either as the point where the load starts to increase from nonzero values or by fitting the initial stage of the loading curve with a suitable function. The uncertainty can be taken either as the uncertainty from the fit or as the step size in the data.

3. **Area function of indenter tip:** The area function can be determined either directly using an atomic force microscope (AFM) or indirectly by evaluating indentations in a reference sample, e.g. fused silica or BK7. In the first case the uncertainty of the area should be determined by standard procedures in AFM. In the second case, all uncertainties which are present for an ordinary indentation measurement contribute as well as the uncertainty of the modulus of the reference sample. If a function is fitted or the data are interpolated, the corresponding uncertainties contribute as well.

4. **Inhomogeneity of the sample:** The sample inhomogeneity can significantly contribute to the overall uncertainty. The roughness of the sample can affect the results as well. The corresponding contribution can be evaluated by statistical evaluation of repeated measurements.

5. **Calibration of the load sensor and the depth sensor:** The load sensor and the depth sensor should be calibrated as described in section 8. A Monte Carlo approach is probably the easiest way although most time consuming. Calibration coefficients should be generated according to their estimate and uncertainty and for each set of calibration coefficients the whole loading curve should be corrected. All corrected loading curves should then be processed by the chosen model and the results should be evaluated statistically. The procedure can be also done separately for the load and depth calibration.

6. **Thermal drift:** Thermal drift must be estimated and corrected for. Depending on the character of the corresponding uncertainty it can be treated either analogously to the uncertainties due to sensor calibration or the noise can be enlarged appropriately.

7. **Compliance of the indenter:** The compliance of the indenter can be determined e.g. by indentation into a material with a very high ratio of $E_{IT}/\sqrt{H_{IT}}$, such as tungsten. The data should be corrected for the compliance. The Monte Carlo approach as in the previous steps can be used to assess the corresponding uncertainty.

Other sources, such as the choice of the fitting interval, details of the fitting procedure, calibration of optical microscope, strain rate and others may contribute as well.

Some sources of uncertainties may be interconnected and their effects may in the end cancel each other. It is necessary, to take this into account and avoid double-counting their contributions to the total uncertainty.

8.6.1 Examples of uncertainty budgets

In this section the concepts of the previous section will be illustrated in detail on two examples: Vickers hardness and Young's modulus determined by the Oliver-Pharr model.

Vickers hardness

The Vickers hardness was measured on a reference block with a certified hardness (742 ± 5) HV1. Vickers hardness is given by

$$HV = \frac{2}{9.80665} \frac{F}{d^2} \sin\left(\frac{136°}{2}\right) \tag{8.11}$$

where $9,806654$ is the gravitational constant, the angle $136°$ is the angle between the sides of the four-sided Vickers tip, F is the load in Newtons and d is the average length of the diagonal in millimeters. The total uncertainty has contributions from the following:

1. Uncertainty of the load, consisting of:
   (a) uncertainty of the calibration,
   (b) deviation from the prescribed load equivalent to 1 kg,
   (c) noise.
2. Uncertainty of the length of the diagonal, consisting of:

   (a) uncertainty of reading,
   (b) uncertainty of calibration.

3. Uncertainty of the tip shape,

4. Inhomogeneity of the sample.

Contributions 1–3 can be evaluated for each measurement separately and then combined with the contribution from the inhomogeneity which is of Type A and should be evaluated statistically.

The uncertainty of the calibration of the load sensor was 0.02 %. The instrumented indentation device didn't allow an exact setting of the resulting maximum load due to feedback issues. The difference between the real value and the desired value was treated as an uncertainty. The noise of the load was estimated as the standard deviation of the arithmetic mean of the load signal during the hold period at maximum load. The uncertainty of the calibration of the optical microscope was 1.5 % and 0.2 % in the x and y direction. The calibration coefficients in the two directions are independent. The uncertainty due to the reading of the diagonal was estimated as 0.3 mm in the worst case.

The calibration of the load is linear

$$F = k_F F^{IIT} \tag{8.12}$$

where F^{IIT} is the indication of the instrument and k_F the calibration constant. The average length of the diagonal is

$$d = \frac{1}{2}(d_1 + d_2). \tag{8.13}$$

where the two diagonals are

$$d_i = \sqrt{d_{i,x}^2 + d_{i,y}^2}, \qquad i = 1, 2. \tag{8.14}$$

The components of the two diagonals are calibrated as

$$d_{i,a} = k_a d_{i,a}^{opt}, \qquad i = 1, 2, \quad a = x, y \tag{8.15}$$

where k_a are the calibration constants and $d_{i,a}^{opt}$ the values read.

Then the Vickers hardness is computed explicitly as

$$HV = A \frac{k_F F^{IIT}}{d^2} \sin\left(\frac{\alpha}{2}\right) \tag{8.16}$$

where $A = \frac{2}{9.80665}$, $\alpha = 136°$ and d is given above.
The law of propagation of uncertainties is in this case a lengthy expression

$$\begin{aligned} u(HV)^2 = & \left(\frac{\partial HV}{\partial k_F}\right)^2 u^2(k_F) + \left(\frac{\partial HV}{\partial F^{IIT}}\right)^2 u^2(F, noise) + \\ & + \left(\frac{\partial HV}{\partial F^{IIT}}\right)^2 u^2(F, setting) + \left(\frac{\partial HV}{\partial \alpha}\right)^2 u^2(\alpha) + \\ & + \sum_{a=x,y} \left(\frac{\partial HV}{\partial k_a}\right)^2 u^2(k_a) + \sum_{i=1,2} \sum_{a=x,y} \left(\frac{\partial HV}{\partial d_{i,a}}\right)^2 u^2(d_{i,} \end{aligned} \tag{8.17}$$

but the individual terms can be easily calculated. All results are gathered in the uncertainty budget in Table 8.1. The most important message we

variable	value	uncertainty	contribution
$u(F; noise)$	-	30 μN	0.002 HV1
$u(F; setting)$	-	20 mN	1.4 HV1
k_F	0.9937	0.0002	0.17 HV1
α	136°	0.1°	0.5 HV1
k_x	0.982	0.0015	1.1 HV1
k_y	1.046	0.002	1.5 HV1
x^{opt}	-	0.1 μm	2.1 HV1
y^{opt}	-	0.1 μm	2.2 HV1
total Type B			3.9 HV1
Type A			1.4 HV1
Type A + B			4.2 HV1

Table 8.1: Table: Example of an uncertainty budget for measurement of Vickers hardness

can take from the uncertainty budget is that the dominant source is the resolution of the optical microscope, which cannot be easily improved. It would be technically possible to reduce the uncertainty due to the setting of the load, by repeating the measurement at different loads. This would come at a cost of extra time and damage to the sample and we can see that the reduction of the total uncertainty would not be worth it.

8.6.2 Young's modulus and indentation hardness

As an illustrative example the uncertainty budget for the determination of Young's modulus and indentation hardness using the Oliver-Pharr model is shown. Several approaches to uncertainty estimation are combined. The measurement was performed by a Berkovich indenter on fused silica. Two loading curves for maximum load 1 mN and 11 mN were used; these are shown in Fig. 8.9

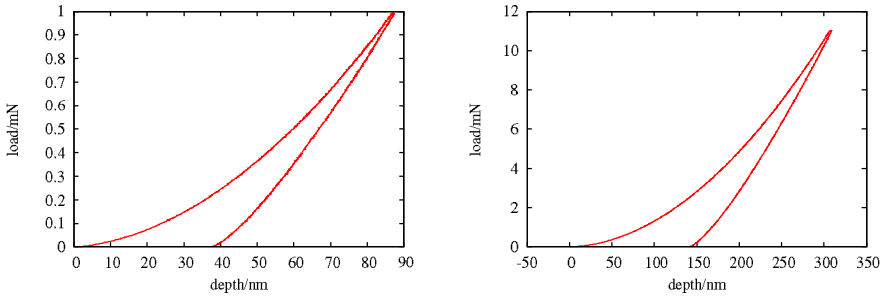

Figure 8.9: Two typical loading curves on fused silica.

The area function of the tip was determined elsewhere as

$$A = 24.5h^2 + p_1 h + p_2 h^{1/2} + p_3 h^{1/4} + p_4 h^{1/8} \tag{8.18}$$

The estimates of the coefficients are

$$\vec{p} = \left(18.34 \times 10^2, 4.25 \times 10^4, 1.88 \times 10^5, 1.19 \times 10^4\right) \tag{8.19}$$

and the estimate of their covariance matrix is

$$U_p = \begin{pmatrix} 4.3 \times 10^5 & -1.5 \times 10^7 & 7.1 \times 10^7 & -6.2 \times 10^7 \\ -1.5 \times 10^7 & 5.5 \times 10^8 & -2.6 \times 10^9 & 2.3 \times 10^9 \\ 7.1 \times 10^7 & -2.6 \times 10^9 & 1.3 \times 10^{10} & -1.1 \times 10^{10} \\ -6.2 \times 10^7 & 2.3 \times 10^9 & -1.1 \times 10^{10} & 9.9 \times 10^9 \end{pmatrix}. \tag{8.20}$$

The noise of the indentation instrument was estimated as 0.1 nm for the depth sensor and 40 nN for the load sensor. The radial correction was applied with an angle $\alpha = 70.3°$ which corresponds to a Berkovich indenter. As explained in [CJ08] the correction angle should lie in the interval

$$\alpha \leq \alpha_r \leq \frac{\pi}{2} - \tan^{-1} \frac{h_p}{a}, \tag{8.21}$$

where h_p is the residual depth and $a = \sqrt{F_{max}/(\pi H)}$ is the contact radius. In general the number of Monte Carlo trials grows with the number of input

variables. Therefore it is preferable to use the law of uncertainty propagation for simpler expressions and use the Monte Carlo method only for more complex relations. In this calculation the uncertainties due to the uncertainty in the area function are treated by the law of propagation of uncertainties, the uncertainty due to noise in the load and depth sensor is treated by Monte Carlo method. Both methods are compared for the contribution due to the uncertainty in Poisson's ratio. The uncertainty related to the radial correction is estimated by other means.

F_{max}	1 mN	11 mN
u(E_r, MC)	0.18 GPa	0.05 GPa
u(E_r, Hess)	0.21 GPa	0.07 GPa

Table 8.2: Comparison of the estimates of the uncertainty of the reduced modulus as determined by the Monte Carlo method and using the Hessian.

Noise of sensors The noise of the sensors is included explicitly in the relations for the contact depth etc. of the Oliver Pharr model and in the fitting procedure of the power law function. The evaluation of the uncertainties of the fitting procedure was performed within the open-source software NIGET, which can be downloaded at www.nanometrologie.cz/niget. The software uses a weighted orthogonal least squares scheme for the fit. The software offers two approaches for the evaluation of the uncertainty: either the Monte Carlo approach or the use of the Hessian approximated by the square of the Jacobian of the function

$$U \propto \left(\mathbf{J}^T\mathbf{J}\right)^{-1}.$$

A comparison for the two loading curves shows that in both case the Hessian method slightly overestimates the uncertainty compared to the Monte Carlo method.

This is in agreement with [MP13] and with [BSDS88] where the authors of the fitting algorithm which is used in the NIGET software showed that the algorithm may overestimate the uncertainty significantly for very small ratios of noise in independent and dependent variable.

The role of the number of trials can be seen from Fig. 8.10 and Fig. 8.11. In Fig. 8.10 the evolution of the standard deviation of the PDF of the reduced modulus is shown. It can be seen that convergence is reached at approx. 30 000 trials. The convergence must be checked for each case separately since it depends on the noise as well as the quality of the fit etc. The rate of convergence for other statistics e.g. mean, confidence interval, may differ and must be evaluated separately. In Fig. 8.11 the time needed for the Monte Carlo computation is shown. The relationship is approximately linear, the time needed for convergence of the uncertainty is around 30 min.

We can also check that the reduced modulus of contact has a normal distribution as shown in Fig. 8.12.

Zero point determination The zero point is the point where the indenter tip touches the sample. It can be determined as the point where the load increases abruptly; a detail of the loading curve close to the zero point is shown in Fig. 8.13. The zero point is chosen at A, however other plausible

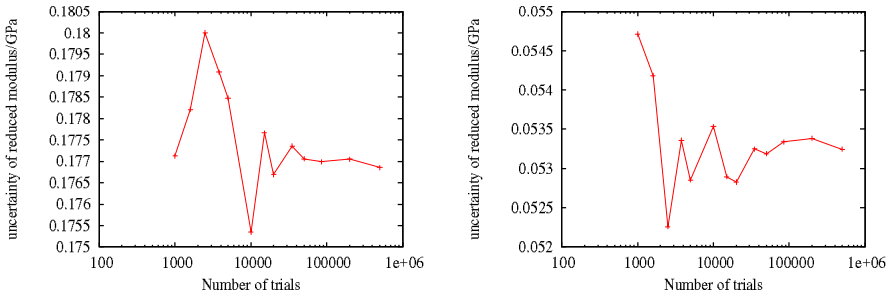

Figure 8.10: The evolution of the standard deviation of the reduced modulus depending on the number of trials for maximum load 1 mN (left) and 11 mN (right).

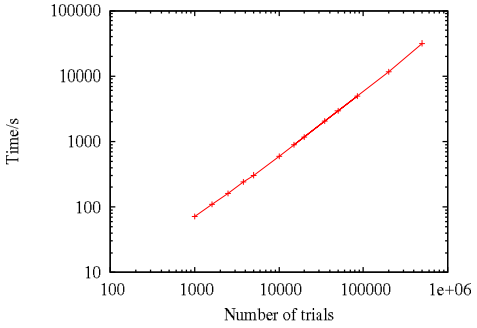

Figure 8.11: The dependence of the time necessary for the Monte Carlo computation on the number of trials used.

choices are B and C.

The resulting reduced moduli which would arise if we chose the points A, B and C are compared in Table 8.3. We can estimate the uncertainty related to the zero point determination as 0.2 GPa. In this example the value is small due to low noise and a high sampling rate.

Uncertainty of area function The uncertainty of the area function can be evaluated by the law of propagation of uncertainties. It contributes to

F_{max}	1 mN		11 mN	
E_r /GPa	A	68.2143	A	69.4423
	B	67.9242	B	69.3437
	C	68.2807	C	69.6294

Table 8.3: Comparison of the reduced modulus for different choices A,B,C of the zero point, as shown in Fig. 8.13.

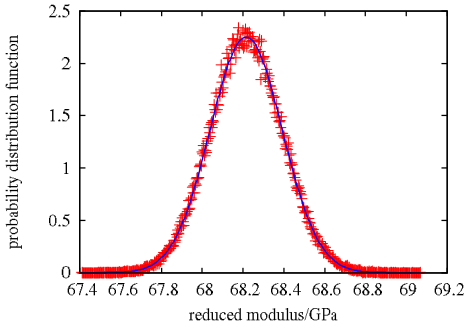

Figure 8.12: The probability distribution function of the reduced modulus as determined by Monte Carlo method and a corresponding normal distribution for comparison.

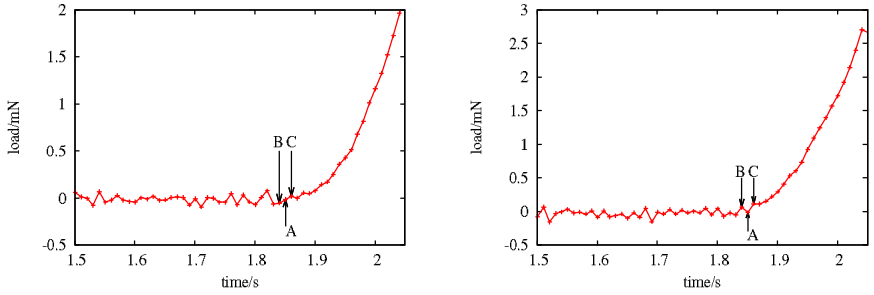

Figure 8.13: The loading curves during the contact between indenter tip and sample for the indentation with maximum load 1 mN (left) and 11 mN (right). The zero point is chosen at A, however other plausible choices are B and C.

F_{max}	1 mN	11 mN
u(A; noise)	250 nm^2	1070 nm^2
u(A; coeff)	2860 nm^2	29530 nm^2
u(A; total)	2870 nm^2	29550 nm^2

Table 8.4: Comparison of the contribution of the contact depth and the area function coefficients to the total uncertainty of the contact area.

the uncertainty of the contact area, together with the uncertainty of the contact depth. As shown in Table 8.4 the uncertainty of the coefficients in the area function dominates.

Radial correction The angle α for the radial correction must lie within the limits given by equation (8.21). For a Berkovich indenter the opening angle of an equivalent cone is 70.3°, the upper limit is $77.0° - 79.0°$. The correction in the reduced modulus itself is fairly small, approx. 3%. The difference between the two results corresponding to the bounding values is even smaller, below 0.2 %. The probability distribution for the reduced modulus can thus be approximated by a uniform distribution. The final uncertainty is very small, 0.03 GPa, and is listed in Table 8.6.

Poisson's ratio The determination of the Young's modulus from the reduced modulus requires some knowledge about the Poisson's ratios of both sample and indenter as well as the Young's modulus of the indenter. Since usually very little is known about the Poisson's ratio and the indenter parameters are taken from literature, it is safer to assume a rectangular distribution in all cases. The law of propagation of uncertainties doesn't work well when variables which have significant contributions have a rectangular distributions. This can be nicely seen by inspecting the probability density function of the Young's modulus for different estimates of the Poisson's ratio when the uncertainty due to the area function coefficients is not taken into account. The probability distributions are shown in Fig. 8.14.

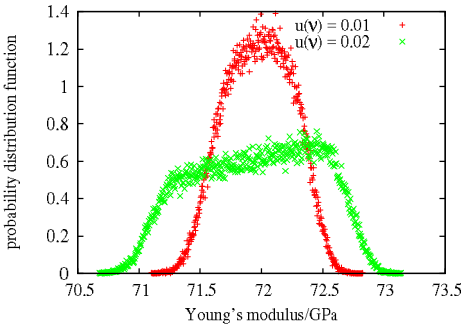

Figure 8.14: Probability density functions for different estimates of Poisson's ratio of the sample ν. The uncertainties of the indenter properties had a much smaller effect, mainly making the decrease at the edges of the distribution less steep.

Checking the corresponding uncertainty budget in Table 8.5, it can be seen that dominating contribution comes from the uncertainty in the area function. However the uncertainty arising from ν cannot be neglected even for fairly optimistic scenarios. The uncertainties due to the unknown properties of the indenter tip are comparable to those due to the noise of the sensors. This underlines the fact, that the uncertainty of the Young's modulus is significantly higher than that of the reduced modulus.

variable	value	uncertainty	contribution
E_r, noise	69.4 GPa	0.07 GPa	0.08 GPa
E_r, area	69.4 GPa	0.9 GPa	0.99 GPa
$E_{indenter}$	1141 GPa	20 GPa	0.11 GPa
$\nu_{indenter}$	0.06	0.1	0.06
ν	0.16	0.01 0.02 0.05	0.24 0.47 1.18

Table 8.5: Uncertainty budget for the contributions to the uncertainty of the Young's modulus.

variable	value	uncertainty	contribution
noise in load	-	40 nN	
noise in depth	-	0.1 nm	0.07 GPa
zero point	-	-	0.2 GPa
coefficients of AF	see (8.19)	see (8.20)	0.9
radial correction	70.3°	1.9°	0.03 GPa
indenter modulus	1141 GPa	20 GPa	0.11 GPa
indenter Poisson's ratio	0.06	0.1	0.06 GPa
sample Poisson's ratio	0.16	0.02	0.5 GPa
total			1.1 GPa

Table 8.6: Uncertainty budget of the Young's modulus. Note that the contributions from noise in load and noise in depth cannot be separated.

Total uncertainty budget of Young's modulus The total uncertainty budget of the Young's modulus for the 11 mN indentation is shown in Table 8.6. We can expect it to be similar for similar situations but caution is necessary.

Acknowledgement This research was funded by Czech Science Foundation project No. 15-17875S. [1]

[1]Submitted: 31.7.2017; Accepted: 31.7.2018

Part III

Application of indentation tests

Chapter 9

Indentation tests of thin films on various substrates

V. Buršíková and L. Zábranský
Department of Physical Electronics, Faculty of Science, Masaryk University, Kotlářská 2, 611 37 Brno, Czech Republic

9.1 Surface Layers - Thin Film Effects

1. The data analysis procedures can assume contact with a homogeneous elastic half space. This requirement is difficult to meet on the nm length scale due to

   - layers of other materials on the surface as natural oxide layers, contaminations, adsrbed water, etc., which typically exist at most of the surfaces;
   - work hardening caused by material polishing, hydration, even "clean" surfaces may have properties unlike their bulk parts.

   There is a question: "How large do the indentations depth have to be to avoid the effects of the above listed surface layers ?"

2. The most frequent requirement is to investigate the properties of a thin film on a substrate. There are other further very important questions: "How small do indentations have to be to avoid effects of the substrate ?", "How it is possible to get the coating properties if we can measure only the average responseof the film-substrate system ?"

3. The length scale of film-substrate interaction depends strongly on

- the relative material properties of film and substrate [LS92,TTN99]
- the properties of interface between the film and the substrate [Mat86, BR87, Bur]

9.2 Soft film on the hard substrate

In the case of the soft film on the hard substrate, the soft film deforms before the harder substrate, it "piles up" (see Fig. 9.1). We may measure the film hardness at the indentation depths approximately equal to the film thickness t_f.

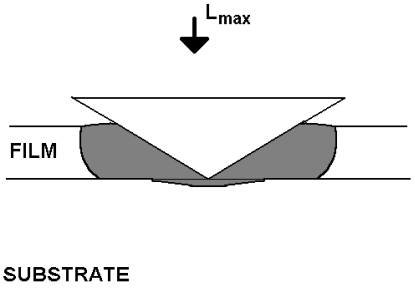

Figure 9.1: Indentation test on the system of the soft film on the hard substrate

9.3 Hard film on the soft substrate

In the case of the hard film on the soft substrate, the substrate may deform plastically earlier than the film itself. We may measure the film properties only when the indentation depth is a small fraction of the film thickness . One often sees "rules-of-thumb" applied. e.g. "indentations to 10% of the film thickness sample the film alone." These rules have no basis in fact, the critical indentation depth, under which the substrate does not influence the measurement [?, B59], depends strongly on the combinations of the coating and the substrate as well as on the interface properties.

9.4 Models for film hardness determination

Effective hardness H_e means the effective indentation resistance of the whole system of thin film on a substrate against plastic deformation.

Different approaches to the calculation of the real microhardness to the of thin films from effective microhardness could be applied:

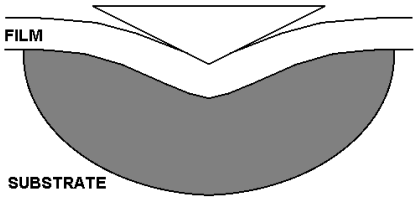

Figure 9.2: Indentation test on the system of the hard film on the soft substrate

For higher depths of the indentation an effective microhardness H_e that characterises the whole system of a film on a substrate is obtained. Different approaches to the calculation of the real microhardness of thin films from effective (composite) microhardness H_e could be applied. Some of them will be briefly reviewed.

9.4.1 Law of mixtures models

Composite model

Bückle [B59] proposed a model to describe the composite character of the measured hardness, where the composite hardness H_e is expressed as a simple average of the film H_f and the substrate hardness H_s:

$$H_e = aH_f + bH_s = H_s + a(H_f - H_s), \tag{9.1}$$

where a and b are functions of the relative indentation depth and a+b=1. The value of a=1, when only the coating effect is measured and its value is 0, when the substrate effects dominates. Bückle expressed the coating effect parameter a as:

$$a = \left[1 - \frac{\exp(h-t)}{\Delta t}\right]^{-1} \tag{9.2}$$

t is the film thickness, h is the depth of indentation, and Δt is the size of the film-substrate transition region. Bückle in [B59] also established a "rule of thumb" that recommends to do the indentation in depths no more than 1/10 of the film thickness to avoid the influence from the substrate. The model 9.1 was modified by Puchi-Cabrera ??:

$$H_e = H_f X_f + H_s X_s, \tag{9.3}$$

where X_f and X_s are volume fractions of coating and substrate, respectively.

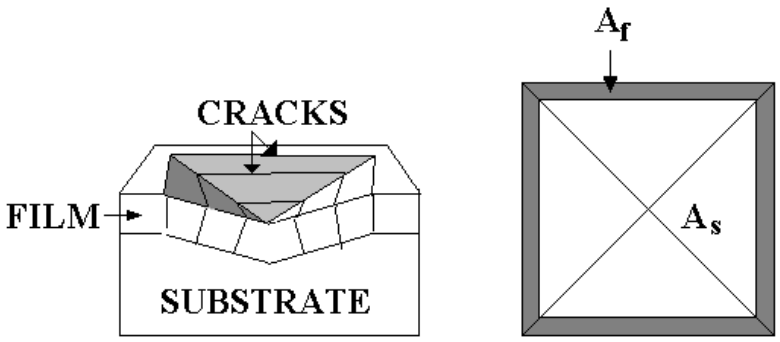

Figure 9.3: Jönnson and Hogmark's model

Area mixture model

Jönnson and Hogmark's model [JH84] uses a geometrical approach to combine the microhardness of film and substrate according to an area mixture model. This method is based on the calculation of the relative contributions of substrate and film to the effective microhardness. By the area mixture model the effective microhardness is expressed as the weighted mean of the substrate hardness H_s and the film hardness H_f:

$$H_\mathrm{e} = \frac{A_\mathrm{f}}{A} H_\mathrm{f} + \frac{A_\mathrm{s}}{A} H_\mathrm{s}, \tag{9.4}$$

where A_f and A_s are the load-supporting areas of the film and substrate and $A = A_\mathrm{s} + A_\mathrm{f}$ is the whole area of an indentation print. An analysis of the geometry leads to

$$H_\mathrm{e} = H_\mathrm{s} + \left[2C \frac{t_\mathrm{f}}{D} - C^2 \left(\frac{t_\mathrm{f}}{D} \right)^2 \right] (H_\mathrm{f} - H_\mathrm{s}), \tag{9.5}$$

where t_f is the film thickness, D is the indentation depth. The formulae 9.5 can be expressed in the form of Bückle's model, where the coatings parameter a is

$$a = 2C \frac{t_\mathrm{f}}{D} - C^2 \left(\frac{t_\mathrm{f}}{D} \right)^2. \tag{9.6}$$

In the case of the Vickers pyramidal indenter with the angle of 136^o between opposing faces $C = 2 \sin^2 116^o$ for hard ductile films (metallic) on the softer

substrate (Model 1) or $C = \sin^2 22^o$ for hard films as SiO_x or DLC on the softer substrate (Model 2). In Model 1 the film is plastically strained to match the shape of the indenting diamond tip. It is assumed, that all strain occurs inside the volume ABC (see Fig. 9.4) and is exerted by a flow stress H_f acting over the area A_f. In the interior indentation the stress is only submitted through the film. In Model 2 the plastic deformation of the film is restricted to the region AB'C as indicated in Fig. 9.4. It is assumed the film accommodates to the indenter by crack formation in the interior of the impression.

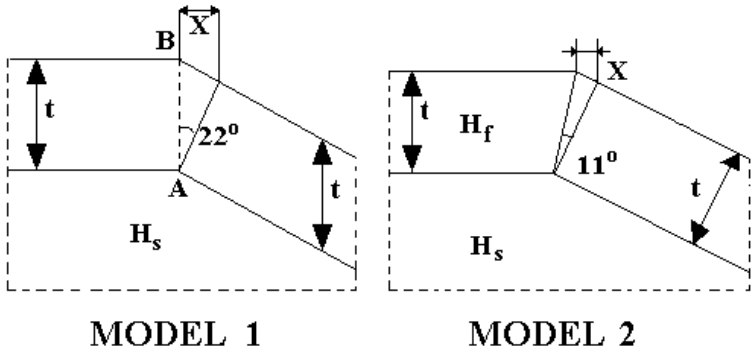

Figure 9.4: Geometry of the indentation prints in Area - Mixture Model 1 and Model 2 [JH84] .

However, the area-mixture model is unsuitable for indentation depths less then the film thickness, since it relies on film cracking to transmit load directly onto the substrate over the central part of the contact area.

Volume mixture model

In the Burnett and Rickerby's model [BR87], known as a volume mixture model, the substrate hardness H_s and the film hardness H_f are combined according to the volumes of plastically deformed materials:

$$H_e = \frac{V_f}{V_f + V_s} H_f + \frac{V_s}{V_f + V_s} H_s \tag{9.7}$$

where V_f and V_s are deforming volumes in the film and the substrate, respectively.

The hemisphere under the indenter is related to the plastic volumes in a spherical cavity model and is affected by the elastic and plastic properties

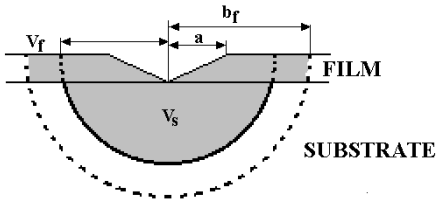

Figure 9.5: Schema of Volume mixture model for $H_\mathrm{f} < H_\mathrm{s}$

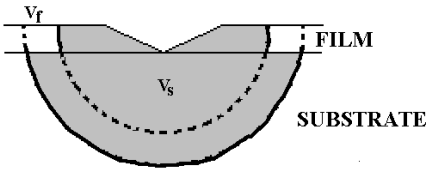

Figure 9.6: Schema of Volume mixture model for $H_\mathrm{f} > H_\mathrm{s}$

of measured materials. Then

$$H_\mathrm{e} = H_\mathrm{s} + \left[k_1 \left(\frac{t_\mathrm{f}}{D}\right)^2 + k_2 \left(\frac{t_\mathrm{f}}{D}\right)^3\right](H_\mathrm{f} - H_\mathrm{s}) \tag{9.8}$$

where $k_1 = 0.759$ and $k_2 = 0.355$ are constants describing the geometry of volume mixture model. However, it was recognised that the plastic radii in each material are influenced by each other and are not simply given by the simple spherical cavity model. Therefore the relation (9.7) was modified. The so called "interface parameter" χ was introduced as a multiplier of one of the term to fit the measured data:

$$H_\mathrm{e} = \frac{V_\mathrm{f}}{V_\mathrm{f}+V_\mathrm{s}} H_\mathrm{f} + \chi^3 \frac{V_\mathrm{s}}{V_\mathrm{f}+V_\mathrm{s}} H_\mathrm{s} \quad \text{for} \quad H_\mathrm{s} < H_\mathrm{f} \tag{9.9}$$

$$H_\mathrm{e} = \chi^3 \frac{V_\mathrm{f}}{V_\mathrm{f}+V_\mathrm{s}} H_\mathrm{f} + \frac{V_\mathrm{s}}{V_\mathrm{f}+V_\mathrm{s}} H_\mathrm{s} \quad \text{for} \quad H_\mathrm{s} > H_\mathrm{f}. \tag{9.10}$$

The interface parameter χ was found to be a strong function of the ratio of the plastic zone radii of the coating and the substrate. Bull and Rickerby [BR90] proposed to use for the interface parameter χ the following relationship:

$$\chi = \left(\frac{E_\mathrm{f} H_\mathrm{s}}{E_\mathrm{s} H_\mathrm{f}}\right)^\mathrm{q}, \tag{9.11}$$

where E_s is the elastic modulus of the substrate, E_f is the elastic modulus of the studied film and q is an adjustment parameter.

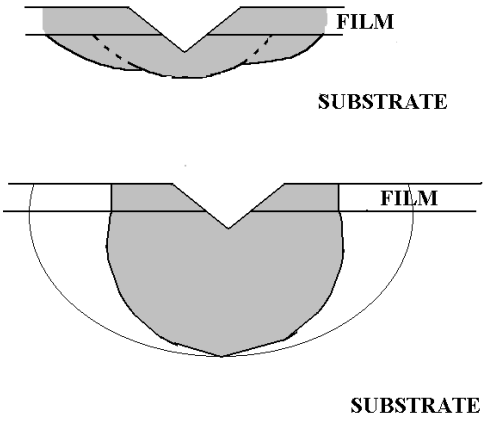

Figure 9.7: Figure illustrating the modified Volume-mixture model

Chicot and Lesage [DC95] developed a model based on two hypothetic systems representing the volumes of the plastic deformation in the film and the substrate under indentation. According to this model the coatings parameter a can be expressed as

$$a = \frac{3}{2}\left(\frac{t}{d}\right)(\pi \tan\xi)^{\frac{1}{3}}\left[\left(\frac{H_{\mathrm{f}}}{E_{\mathrm{f}}}\right)^{\frac{1}{2}} + \left(\frac{H_{\mathrm{s}}}{E_{\mathrm{s}}}\right)^{\frac{1}{2}}\right] - 2\left(\frac{t}{d}\right)^{3}(\pi \tan\xi)\left[\left(\frac{H_{\mathrm{f}}}{E_{\mathrm{f}}}\right)^{\frac{3}{2}} + \left(\frac{H_{\mathrm{s}}}{E_{\mathrm{s}}}\right)^{\frac{3}{2}}\right], \tag{9.12}$$

where ξ is the indenter semi-angle 74^{o}.

9.4.2 Cavity model

Ford's [For94] model is based on the analytical solution for the stress and strain fields around a pressurised coated spherical cavity, taking into account elastic and perfectly plastic deformation. The theory predicts a critical indenter penetration up to which the hardness is reasonably unaffected by the substrate properties, but beyond which the hardness changed rapidly.

The model is divided into two parts. The first part is concerns the case, where the whole of the film and the substrate up to an radius c_s is plastic and beyond this radius the substrate is elastic. The second part concerns

the regime where the substrate is completely elastic, but the film is plastic within a radius c_f and elastic beyond.

For small D/t_f the effective microhardness is given as follows

$$H_{\mathrm{e}} = H_{\mathrm{s}} + (H_{\mathrm{f}} - H_{\mathrm{s}}) \left[\frac{2Kd}{3D} - K^2 \left(\frac{t_{\mathrm{f}}}{D} \right)^2 + \mathcal{F} \left(\frac{t_{\mathrm{f}}^3}{D^3} \right) \right] \quad (9.13)$$

$$K = \frac{\sin\phi}{(\frac{2}{\pi})^{1/2} \tan^{2/3}(\phi)} \quad (9.14)$$

where $\mathcal{F}$ is a function of $\left(\frac{t_{\mathrm{f}}}{3} D^3\right)$ and ϕ is half the angle between opposite faces of a pyramidal indenter.

The following examples of thin films hardness determination were obtained on thin films deposited by plasma enhanced chemical vapour deposition (PECVD) from octamethylcyclotetrasiloxane/oxygen feeds. The results on the effective hardness measurements are shown in Fig. 9.8. The effective hardness dependences on the relative depth were fitted by several empirical models. The "Area-mixture" and the "Volume-mixture" model were used for relative depths greater than 1. For lower values of relative depths the "Cavity model" for elastoplastic films was used. The "Area-mixture" model gave better fits, if the differences between the film and substrate hardness were not higher than 40 % of the substrate hardness. For higher differences the "Volume-mixture" model appeared as more suitable. On the other hand, the "Volume-mixture" model gave worse fits for lower differences in the hardness. Fig. 9.9 shows the results of the fitting for films prepared at different applied powers and negative self bias voltages. There was a slight increase in film hardness with applied power and negative self bias. The film hardness was about 7 GPa, only for applied power 50 V was observed lower value of film hardness $H_{\mathrm{f}} = 4.2$ GPa. In this case more intensive debonding around the indentation print was observed. As it can be seen in Fig. 9.9, the dependence of the calculated film hardness on the relative depth could be taken as constant in the range of the experimental errors.

Energy expenditure model

The model developed by Korsunsky et al. is based on energy expenditure during the indentation process. This model describes either plasticity or fracture dominated behaviour:

$$H_{\mathrm{e}} = H_{\mathrm{s}} + \frac{H_{\mathrm{f}} - H_{\mathrm{s}}}{1 + \mathrm{k}\beta^2}, \quad (9.15)$$

where $\beta = \frac{D}{t_{\mathrm{f}}}$ is the relative indentation depth and k is a dimensionless transition parameter. Tuck [ea01] and coworkers modified equation of Korsunsky

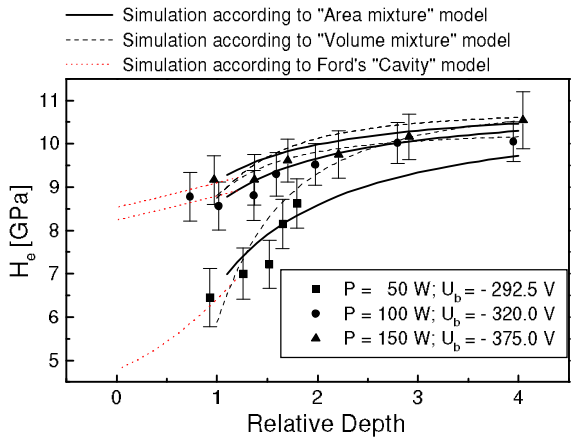

Figure 9.8: Dependence of the effective hardness H_{e} on the relative indentation depth.

in the following way:

$$H_{\mathrm{e}} = H_{\mathrm{s}} + \frac{H_{\mathrm{f}} - H_{\mathrm{s}}}{1 + \mathrm{k}\beta^{X}}, \tag{9.16}$$

where the power exponent X depends on the deformation mode and the geometry of the indentation test. The advantage of this model is, that it allows more accurate fitting of the experimental data, than the previous model.

Finite Element Modelling (FEM) based model

Battacharia and Nix found a good correlation between their finite elements model and the following expression:

$$H_{\mathrm{c}} = H_{\mathrm{s}} + (H_{\mathrm{f}} - H_{\mathrm{s}}) \exp(-\alpha h_{\mathrm{rel}}^{n}), \tag{9.17}$$

where α is a fitting constant, h_{rel} is the relative indentation depth, n is 2 for soft film on the relatively hard substrate and 1 for hard film on relatively soft substrate. The 9.17 is purely empirical, however it was found to correlate well with the finite element simulations [?]. In Figs. ??,??, ?? examples of the application of the model developed by Battacharya and Nix are shown.

Analysis of load-penetration curves

The influence of the substrate from elastoplastic film model is given by the following relationship

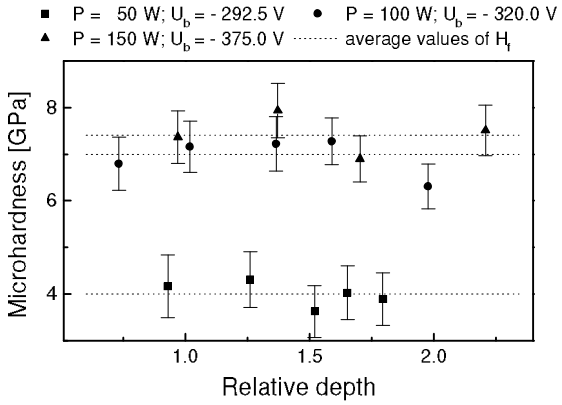

Figure 9.9: The dependence of the calculated film hardness H_f on the relative indentation depth and its average values for different applied powers and bias voltages.

$$L_{corr} = G\frac{(1+\nu_f)E_f}{27(1-\nu_f)^2\sigma_{yf}}(\frac{a}{t})^3 \tag{9.18}$$

where $\frac{t}{a}$ for pyramidal indenter is

$$\frac{t}{a} = 1 + \frac{h}{d}\frac{sin\phi}{(\frac{2}{\pi})^{\frac{1}{3}}tan^{\frac{2}{3}}\phi} \tag{9.19}$$

Acknowledgement This research was funded by the Ministry of Education, Youth and Sports of the Czech Republic, project LO1411 (NPU I) and by by Czech Science Foundation project No. 15-17875S [1]

[1]Submitted: 31.7.2018; Accepted: 20.12.2019

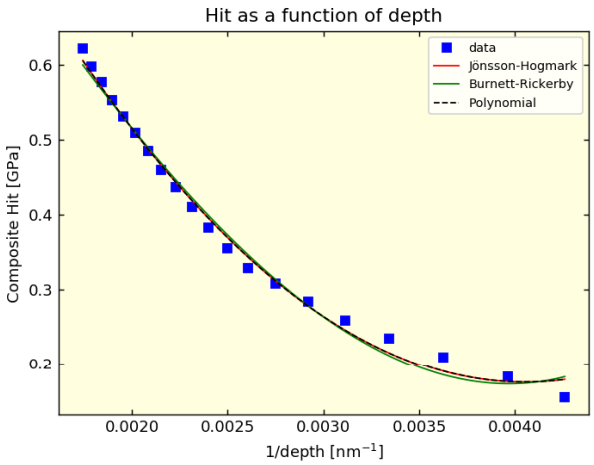

Figure 9.10: Example of application of the model developed by Battacharya and Nix.

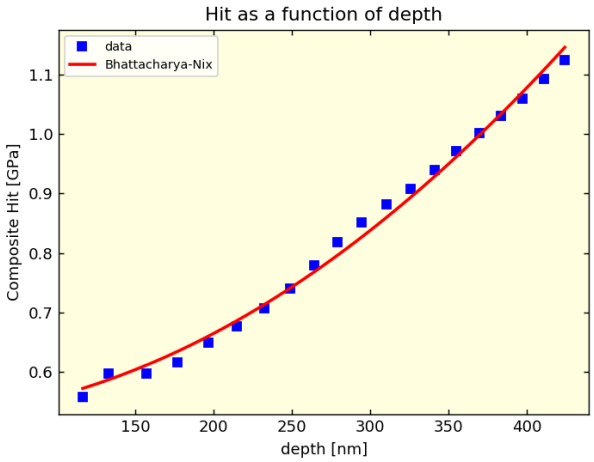

Figure 9.11: Example of application of the model developed by Battacharya and Nix.Soft coating on hard substrate.

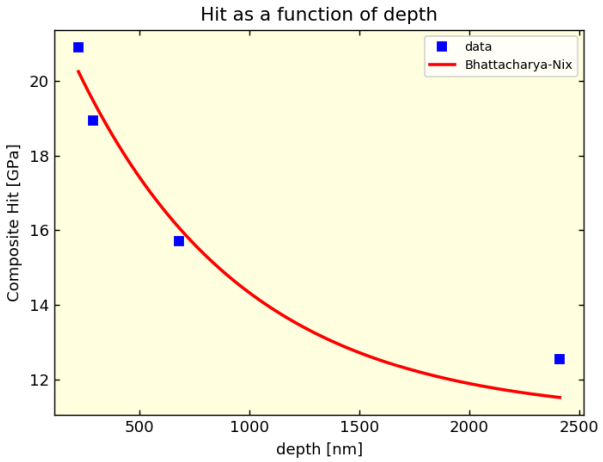

Figure 9.12: Example of application of the model developed by Battacharya and Nix. Hard coating on soft substrate.

Chapter 10

Study of Indentation Induced Defects in Thin Films

V. Buršíková
Department of Physical Electronics, Faculty of Science, Masaryk University, Kotlářská 2, 611 37 Brno, Czech Republic

10.1 Basic terms

The indentation test can induce a wide range of failures, namely dislocation creation, cracking, chipping, phase transformation, mechanical twinning and in case of thin films also buckling and delamination.

Cracking is a class of mechanical failures occurring usually in brittle materials as a mechanism to release indentation-induced stresses by forming cracks. These cracks can develop at the surface or sub-surface, can be lateral or longitudinal. In composite materials (including a two-composite system of thin film and substrate) in which the surface layer is under tensile stress, the stress can propagate cracking away from the initial crack-forming indentation until the whole surface is cracked in a network-like manner (fig. 10.1b, 10.1a).

Peeling is the process of forming 'peels' of the surface layer, which occurs when a surface-wide mesh-like cracking occurs while the surface layer is under compressive stresses able to partially overcome interlayer adhesion along the cracks (fig. 10.1c).

Delamination is a mode of failure common in composite materials and materials with the ability to form a mica-like structure when loaded. Delamination happens mostly during unloading, though the mechanisms involved

(a) Microcracking propagated by tensile stresses (SEM imaging).

(b) Detail of intersecting cracks (SEM imaging).

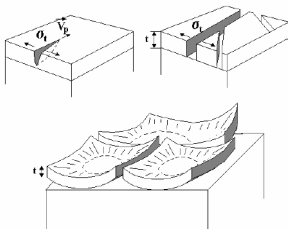

(c) Peeling schema.

Figure 10.1: Cracking and delamination.

can differ. For example, if loading deforms the surface layer elastically, while the sub-surface layer plastically. Upon unloading, atoms of the surface layer will reassume their original position, but subsurface atoms will not. Another mechanism can be based on an inwards-collapsing response of the surface layer (fig. 10.2a). In most severe cases of delamination material can be actually removed during unloading. This type of failure is called chipping (fig. 10.4).

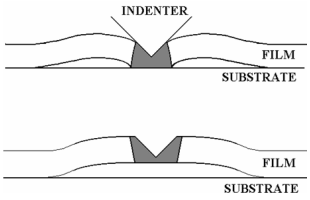

(a) Loading delamination scheme.

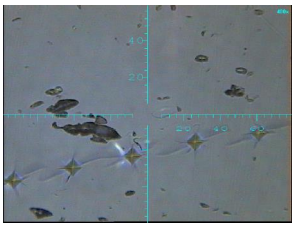

(b) Anisotropic tensile cracks

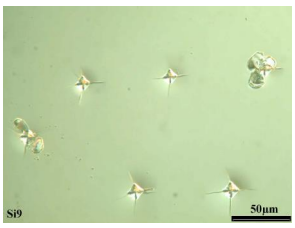

(c) Cracks, delamination, chipping

Figure 10.2: Indentation induced delamination, cracking, buckling, chipping.

Buckling (fig. 10.3) is a form of delamination that requires the presence of compressive stresses in the surface layer. These stresses can be indentation induced or, which is more likely, can be present prior external forces were applied (i.e. thin film coatings with residual cooldown stresses).

Different failures can occur at the same time. In that case, failure induced effects appear side by side and can combine. A measure quantifying failures is the fracture toughness.

There is a method suggested by Joslin and Oliver to correct for pileup without need of imaging. The contact area should be eliminated according to the following formula:

$$\frac{L_{\max}}{S^2} = \frac{1}{\beta^2}\frac{\pi}{4}\frac{H}{E_r^2},$$

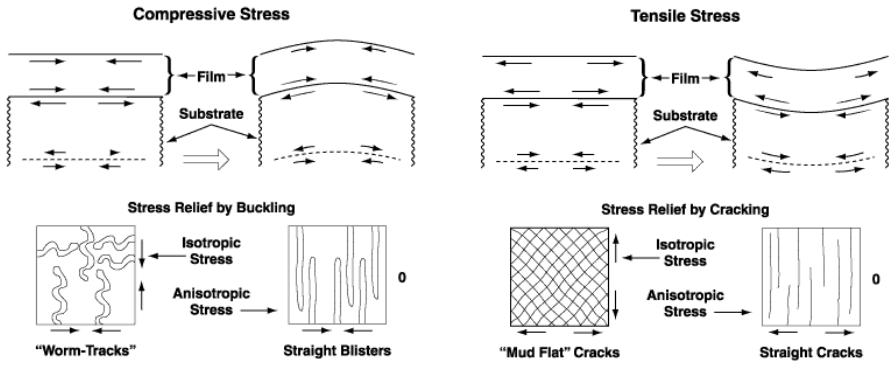

Figure 10.3: Compressive and tensile stresses schema.

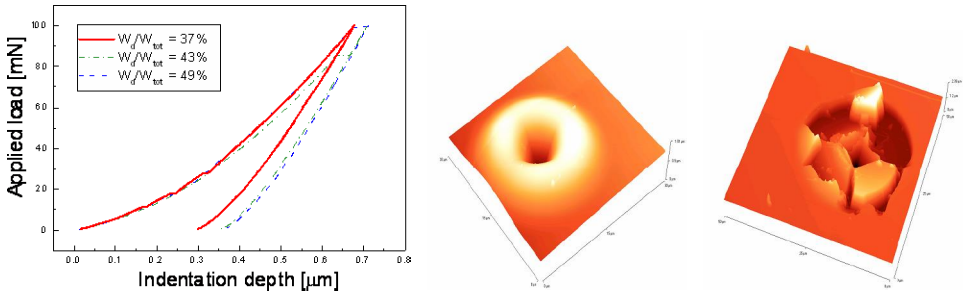

(a) II measurement with delamination (b) Delamination (AFM) (c) Chipping (AFM)

Figure 10.4: Indentation induced fractures in thin film coatings with tensile stress.

where L_{max} is the maximum indentation load, S is the unloading stiffness, E_r is the reduced elastic modulus, H is the hardness and β is a constant and depends on the geometry of the tip.

An other issue are indentation induced phase transformations caused by applied pressure and shear forces inside the material. The later is often considered more important because transformations often involve changes of shape (and thus changes of symmetry as well), while pressure can only effect the material's density. Shear strains and pressure can help the solid pass over the energy barrier that separates its phases - even when the thermal activation of the material is rather insignificant. Shear strains destabilize the electronic structures of the solid and reduce the energy gaps to such an extent, that they can be overcome by zero-point vibration energies. Pressure can have both a stabilizing and a destabilizing effect.All in all, phase transformations are troublesome in DSI measurements because they may cause material property differences in the loading and unloading stage of a single measurement. Furthermore they couple with other prob-

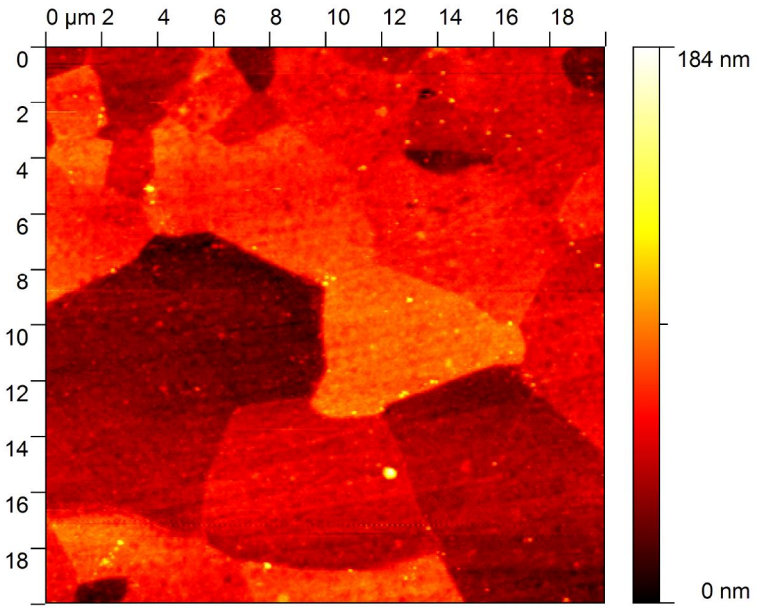

Figure 10.5: AFM image of the tested Aluminium sample surface

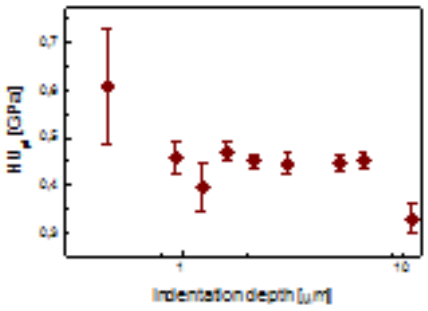

Figure 10.6: Dependence of the hardness on the indentation depth. There is an increase of the hardness at low indentation depth due to higher hardness of the oxide layer.

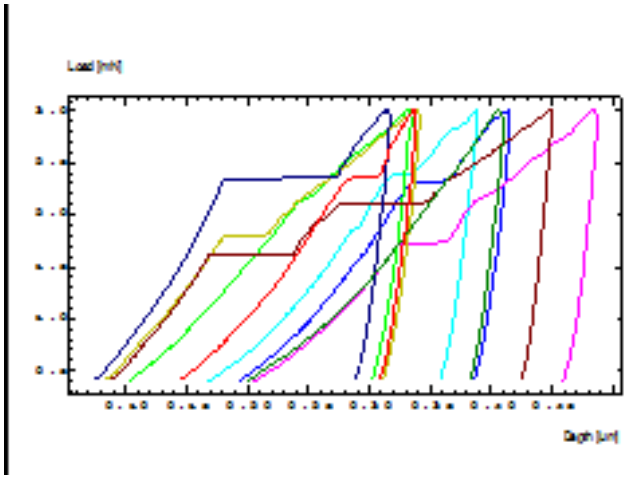

Figure 10.7: Influence of oxide layer on the load penetration curves obtained on aluminium sample covered by oxide layer. The jumps on the loading curves were created due to cracking of the oxide layer.

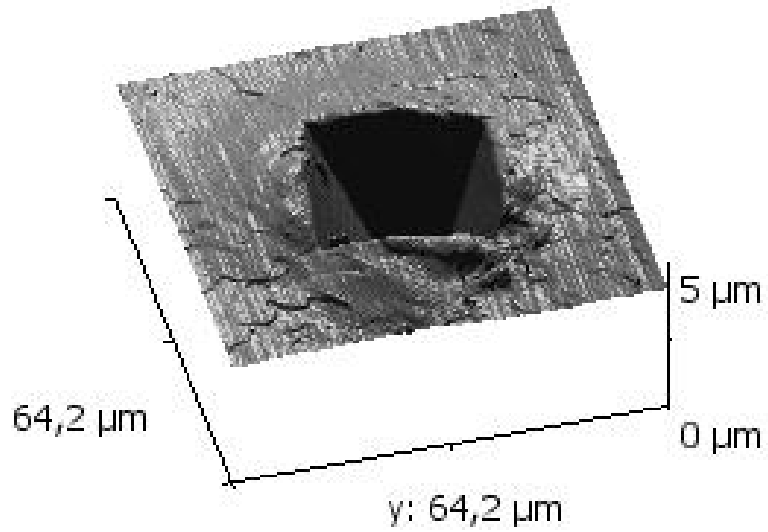

Figure 10.8: AFM image of the indentation print obtained on Aluminium sample.

lematic effects such as metallization of semiconducting crystals. There are several ways of detecting and imaging different phases created due to indentation induced phase transformation. I.e. optical microscopy, SEM, EBSD microscopy (Electron Backscattered Diffraction), LFM (lateral force)and MFM (modulated force)mode in AFM, Raman spectroscopy or RTG diffraction methods.

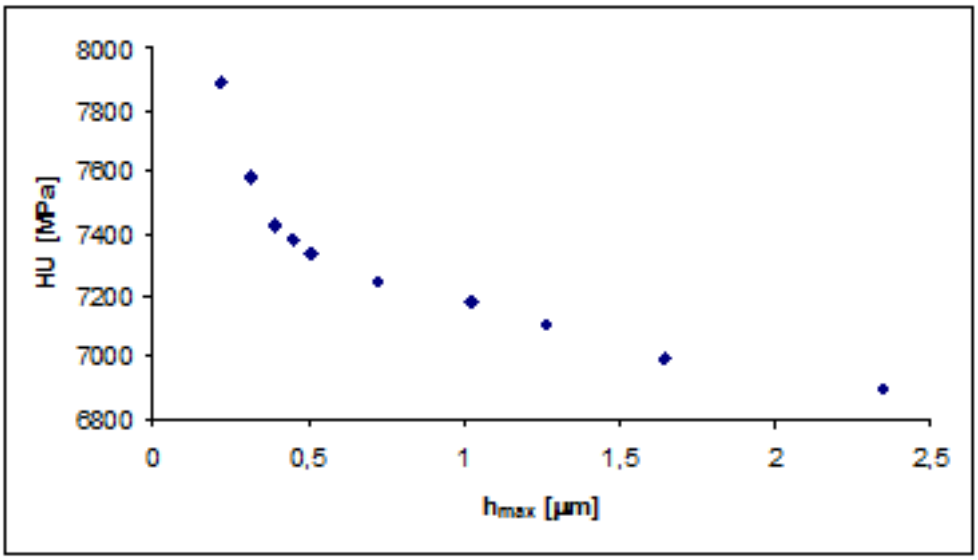

Figure 10.9: Dependence of universal (Martens) hardness of single crystalline silicon <111>on maximum indentation depth. Please note that the error bars are not displayed because their span is much smaller then the size of markers in this plot. The depth dependence of the hardness is caused by indentation induced phase transphormation (from cubic diamond structure to metallic β-Sn structure) at low depths and by cracking at larger depths >500nm.

According to recent results, silicon exhibits multiple phase transformation during nano- or microindentation [5]. The sequence during increasing load: from cubic diamond structure to metallic β-Sn structure. During decreasing load: from metallic β-Sn structure to romboedric and body centered cubic structure or in case of rapid unloading from metallic β-Sn structure to amorphous structure.

A different shape change connected with DSI measurements is the crystal twinning. Twinning is an effect occurring at constant density when two separate crystals share some of the same crystal lattice points in a symmetrical manner. The result is an inter-growth of two separate crystals in a variety of specific configurations. Materials most prone to twinning are crystals with low stacking fault energy

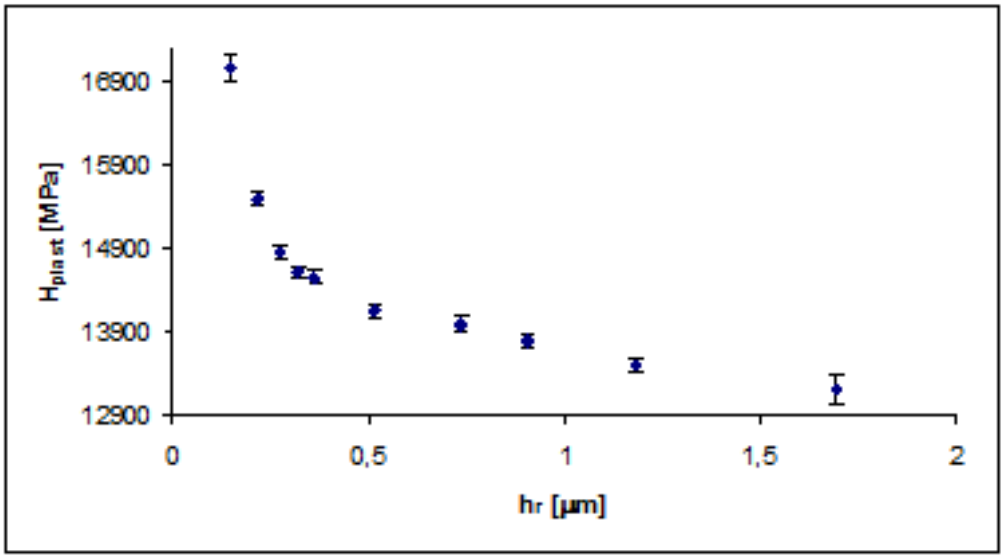

Figure 10.10: Dependence of corrected hardness on corrected indentation depth for single crystalline silicon <111>sample.

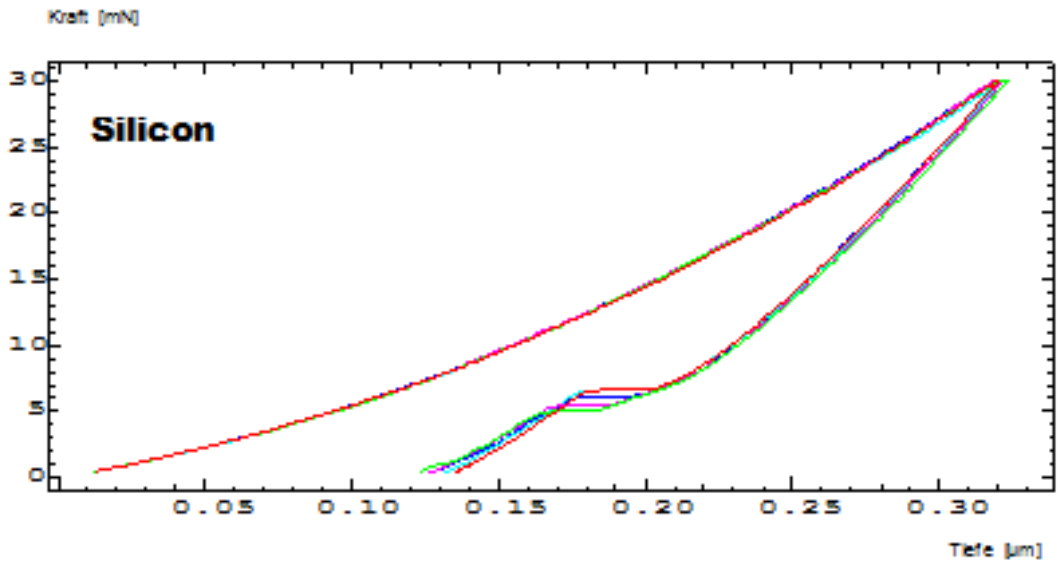

Figure 10.11: Load-penetration curves for indents on Si illustrating the discontinuity during unloading caused by phase transformation of silicon.

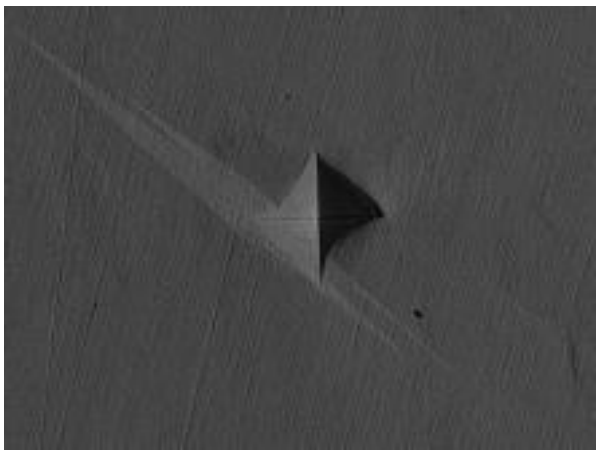

Figure 10.12: SEM image of indentation print in zinc sample. The non-regular shape of the indentation print is caused by indentation induced twinning.

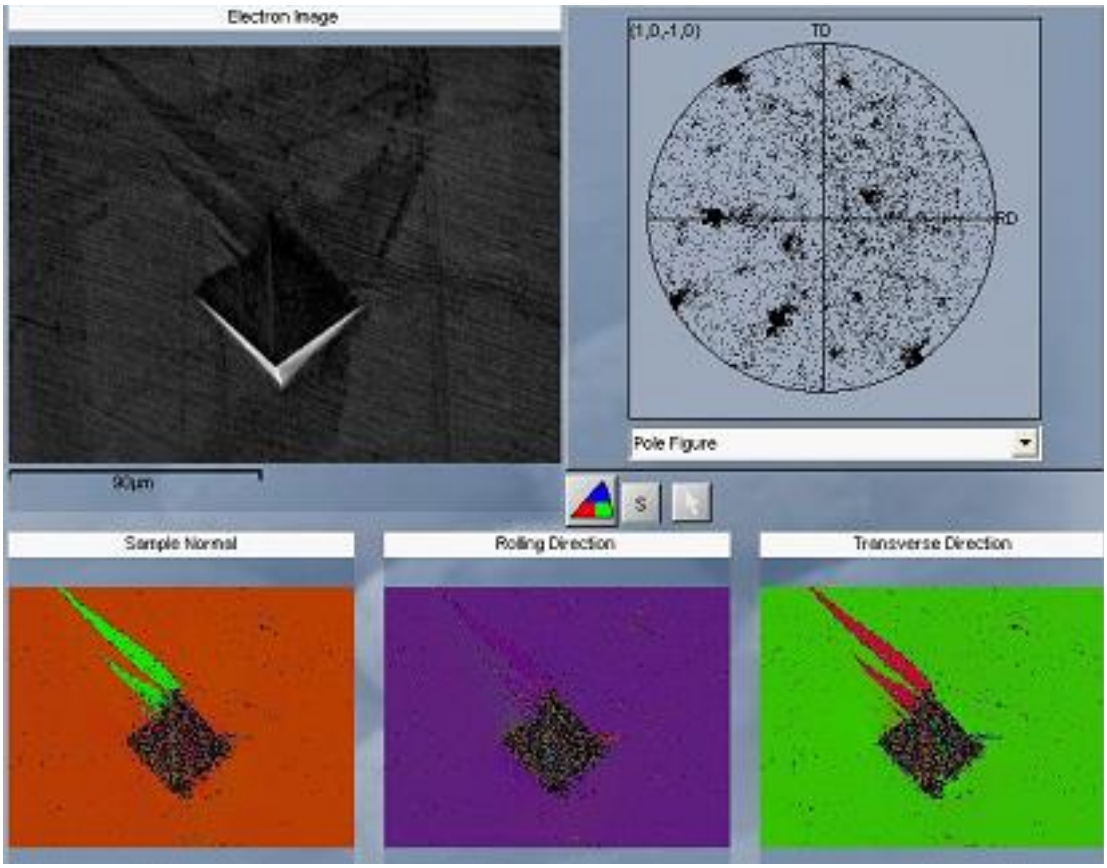

Figure 10.13: Visualisation of the indentation induced twinning in zinc using electron backscattered diffraction (EBSD) method.

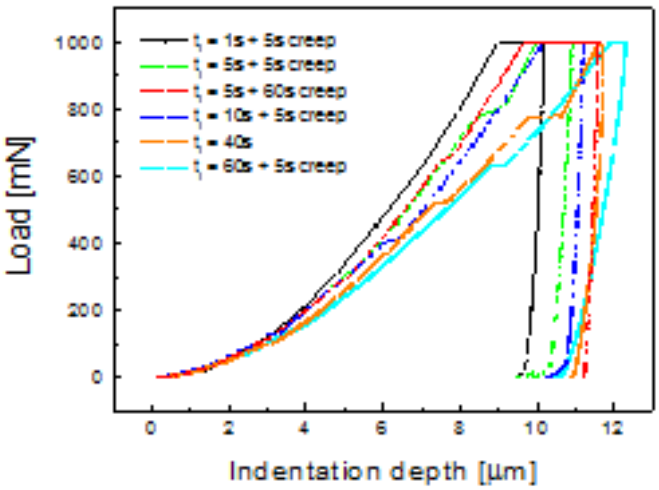

Figure 10.14: The indentation induced twinning effect in zinc significantly depended on the loading rate. The jumps on the oading curve were caused by creation of twins.

Last but not least, DSI probing can lead to irreversible collapses (such as cracking and delamination. These effects are characterized by a significant change of the irreversible energy. Under the term irreversible energy we assume the sum of plastic deformation and fracture energies $W_{irr}=W_{pl}+W_{fr}$. The following figure shows cracking of the silicon sample.

Because of its brittleness and phase transformation, the single crystalline silicon is not suitable as standard for calibration of the indentation instruments. Its usage as substrate material is also problematic.Thin films deposited on silicon substrate may crack not due to their low fracture toughness, but due to low fracture tougness of silicon.

10.2 Summary

The interpretation of the nanoindentation data may be difficult, as residual stresses can modify the contact area and consenquently can invalidate the standard procedures of analysis. Work hardening, phase transformation, mechanical twinning or cracking in the deformed zone may substantially influence the loading-unloading behaviour. Especially at nanoscale it is necessary to use complementary methods such as scanning electron microscopy, electron backscattered diffraction technique, atomic force microscopy etc. in order to monitor the changes in the studied material.

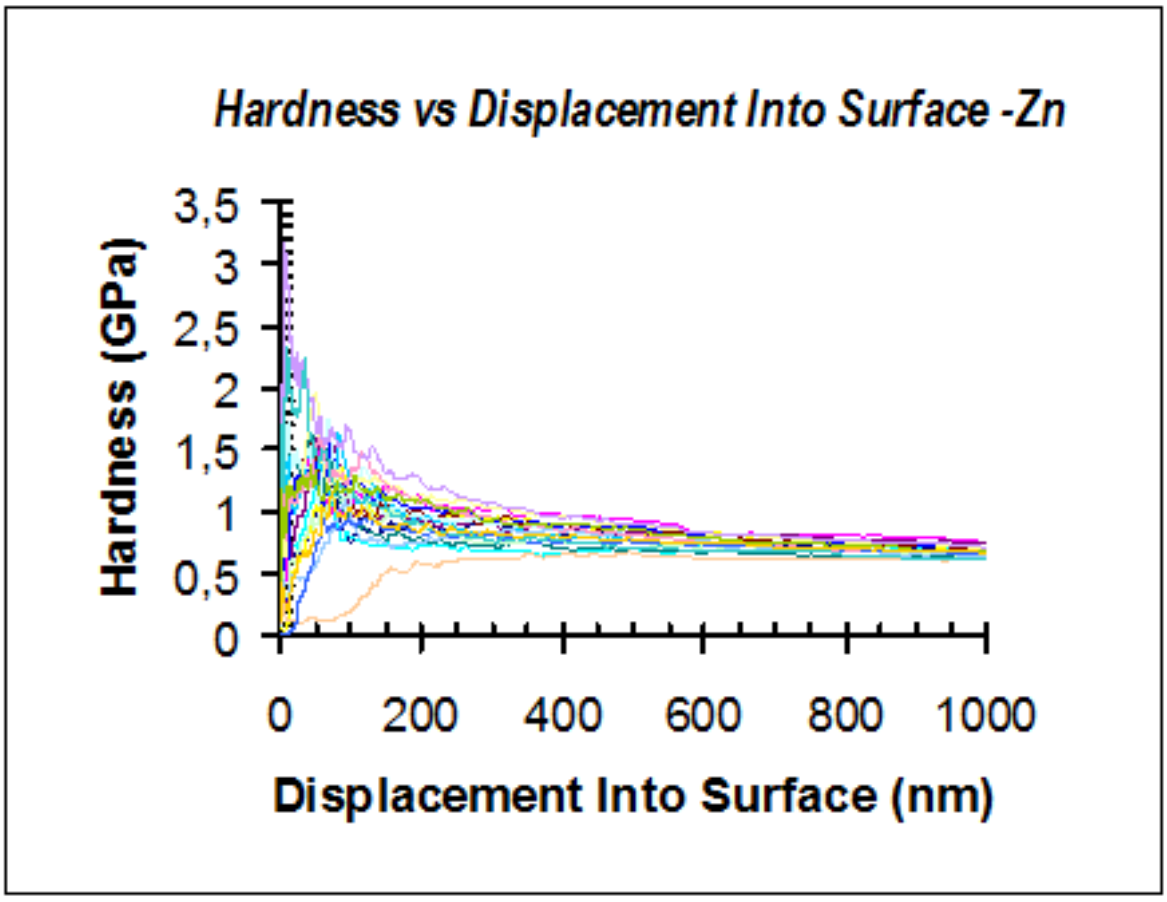

Figure 10.15: The indentation induced twinning influenced also the results obtained on hardness of the zinc sample using the continuous stiffness measurements. The hardness measurement shows high scatter up to 300 nm of the indentation depth.

Figure 10.16: Part of the loading curves in the region of load from 0 to 0,4mN illustrating the effect indentation induced twinning (The curves were obtained using Nanoindenter XP).

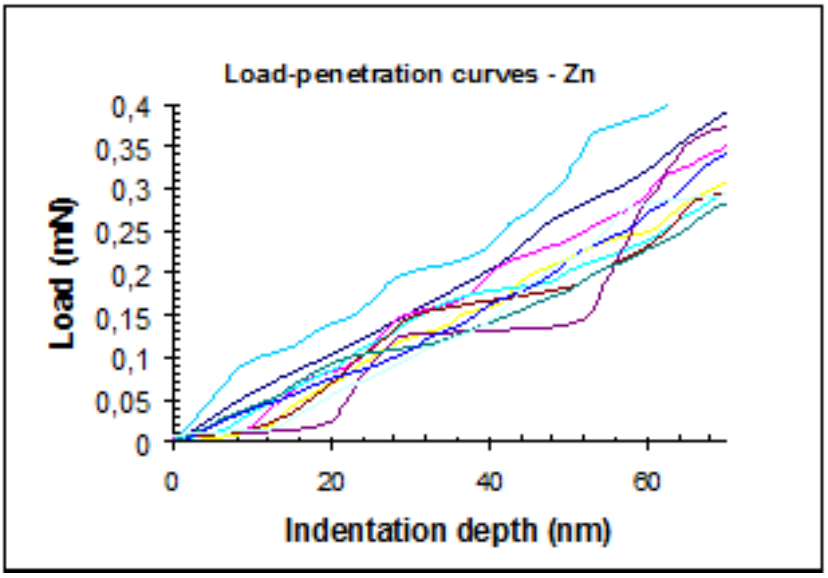

Figure 10.17: Indentation induced fracture (craking and chipping) of the single crystalline silicon sample.

The interface between the film and the substrate can slip or fracture. Indentation methods can be used to measure the adhesion. Adhesion of thin films is difficult to quantify in a physically meaningful way. Recently, the indentation technique has been developed for thin film adhesion measurement. This technique is unique in being able to determine in one experiment the two adhesion parameters required to uniquely specify interfacial strength [Mat86].

The indenter is loaded normally onto the film, which deforms and displaces laterally. This lateral motion of the film results in a shear stress across the interface which, at sufficiently high indenter loads, causes an interfacial crack to initiate and subsequently propagate. If the film or the substrate is transparent,the interfacial crack could be observed. If the crack is not visible by direct observation it may be detected by ultrasonic imaging or acoustic emission.

The interfacial strength needs to be specified by two independent parameters. The first is usually called the interfacial resistance, is analogous to the fracture toughness of a bulk solid and is a measure of the energy required to create a unit area of interfacial crack. The interfacial fracture resistance is normally measured by determining the stress or load required to create a unit area of interfacial crack. The resistance is then calculated from energy balance considerations.

The second parameter is a strength parameter, which depends on the fracture resistance and strength-controlling defects as well as on the nature of strength measurement technique (shear, tension, etc.) and on any residual deposition stresses in the film.

If an interface is found to be unacceptably weak then this could be caused either by having an inherently weak interface because of poor bonding (i.e. low fracture resistance), or by having large interfacial defects. The indentation technique is unique in its ability to measure both adhesion parameters in one experiment.

The indenter is loaded onto the film until a critical load is reached where fracture is initiates; further loading causes the interfacial crack to grow stably. Thus, this test is able to examine both the initiation and the propagation stages of fracture.

In contrast, other test techniques look only at one stage. For example, the p̈in pull-̈test is able to examine initiation only since pull-off represents the onset of catastrophic failure. On the other hand, thep̈eel-̈test examines the stable propagation of an interfacial crack. Thus, these two tests measure quite different parameters since the initiation stage is determined by the strength of the interfacial fracture resistance.

In [Mat86] the indentation test is introduced as possible technique for interfacial failure measurement.

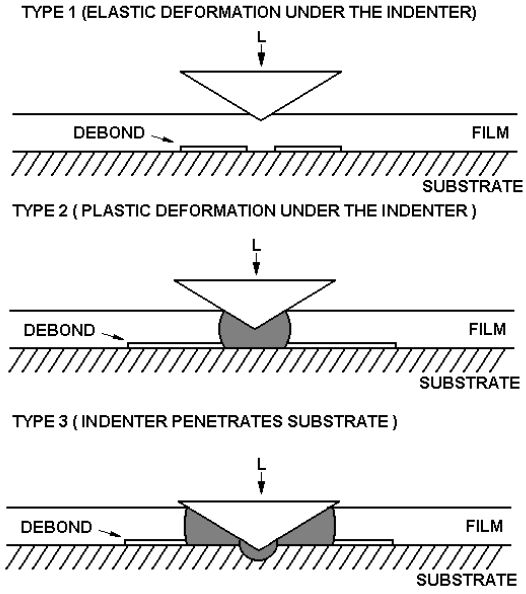

Figure 10.18: Figure illustrating the three stages of the indentation induced interface failure

The initiation stage of failure

Matthewson [Mat86] and Ritter et al. [JRL89] studied the adhesion of a range of thin polymeric films on rigid substrates using the indentation technique and found that, even though the details of the film deformation were variable, the adhesive failure is initiated in essentially the same way for all systems studied. The failure initiates, when the interfacial shear stress at the contact edge exceeds some initial value, σ_c. We can calculate the critical interfacial shear strength σ_c from measurements of the critical load to initiate debonding, L_c, and the contact geometry at the debonding but the exact relationship depends on the type of deformation of the film beneath the indenter which may range from fully elastic to predominantly plastic. Ritter [JRL89] identified three distinct type of behaviour, shown schematically in Fig **??**.

Type I The deformation of the film remains elastic up until debonding occurs.

Type II The film deformation is predominantly plastic or irreversible at debonding but the film is not penetrated.

Type III The indenter penetrated the film before debonding occurs so that some indentation load is supported directly by the substrate.

The failure type for a given system depends on the film thickness and the adhesion and the indenter sharpness. Blunt indenters and thick, poorly adhering films favour Types I and II, while sharp indenters or thin, well-adhering films favour Type II and III. Pointed indenters, such as the Vickers pyramid indenter, are infinitely sharp and produce plastic deformation and can be used to produce mainly Type II and III. Between these types are regions of mixed behaviour, particularly between Types I and II, when the film deformation is elastoplastic.

Acknowledgement This research was funded by the Ministry of Education, Youth and Sports of the Czech Republic, project LO1411 (NPU I) and by by Czech Science Foundation project No. 15-17875S [1]

[1]Submitted: 31.7.2018; Accepted: 20.12.2019

Bibliography

[A.E94] R. Vestergaard A.E.Giannakopoulos, P.-L. Larsson, Int. J. Solids Struct. **31** (1994), 2679.

[B$\ddot{5}$9] H. Bückle, *Progress in microindentation hardness testing*, Metall. Rev **4** (1959), 49–100.

[BL97] et. al. B.N. Lucas, MRS Symp. Proc. **436** (1997), 233.

[Bol] Bolschakov.

[BR87] P. J. Burnett and D. S. Rickerby, *The mechanical properties of wear-resistant coatings i, ii: Modelling of hardness behaviour*, Thin Solid Films **148** (1987), 41–57.

[BR90] S. J. Bull and D. S. Rickerby, *New developments in the modelling of the hardness and scratch adhesion of thin films*, Surface and Coating Technology 42 **42** (1990), 149–164.

[BSDS88] P. T. Boggs, C. H. Spiegelman, J. R. Donaldson, and R. B. Schnabel, *A computational examination of orthogonal distance regression*, Journal of Econometrics **38** (1988), 169–201.

[BSP+10] A. C. Barone, M. Salerno, N. Patra, D. Gastaldi, E. Bertarelli, D. Carnelli, and P. Vena, *Calibration issues for nanoindentation experiments: Direct atomic force microscopy measurements and indirect methods*, Microscopy Research and Technique **73** (2010), 996–1004.

[Bur]

[CJ08] T Chudoba and N M Jennett, *Higher accuracy analysis of instrumented indentation data obtained with pointed indenters*, Journal of Physics D: Applied Physics **41** (2008), no. 21, 215407.

[Coh94] M. L. Cohen, Solid-State Commun. **92** (1994), 45.

[CVZK11] Anna CampbellovĂ˘, Miroslav Valtr, Jaroslav ZĹŻda, and Petr Klapetek, *Traceable measurements of small forces and local mechanical properties*, Measurement Science and Technology **22** (2011), no. 9, 094007.

[CĹKBss] Anna CharvĂ˘tovĂ˘ Campbell, Radek Ĺ lesinger, Petr Klapetek, and Vilma BurĹ˘ĂkovĂ˘, *Atomic force microscopy measurements of the area function of a sphero-conical tip*, Key Engineering Materials (in press).

[DC95] J. Lesage D. Chicot, *Absolute hardness of films and coatings*, Thin Solid Films **254** (1995), 123–130.

[DN86] M.F. Doerner and W.D. Nix, J. Mater. Res. **1** (1986), 601.

[ea01] J.R. Tuck et al, *Indentation hardness evaluation of cathodic arc deposited thin coatings*, Surface and Coating Technology **139** (2001), 63–64.

[For94] I. J. Ford, *A cavity model of the indentation hardness of a coated substrate*, Thin Solid Films **245** (1994), 122–131.

[GAM81] P.R. Lawn G.R. Anstis, P. Chantikul and D.B. Marshall, J. Am. Ceram. Soc. **64** (1981), 533–581.

[GAS05] U. Hangen G. Aldrich-Smith, N. M. Jennett, *Direct measurement of nanoindentation area function by metrological afm*, Z. Metallkd. **96** (2005), 1267 –1271.

[GHL10] A. Germak, K. Herrmann, and S. Low, *Traceability in hardness measurements: from the definition to industry*, Metrologia **47** (2010), 59–66.

[GMPB92] W. C. Oliver G. M. Pharr and F.R. Brotzen, J. Mater. Res. **7** (1992), 613.

[GS78] M. Adam G. Sines, Fracture Mechanics of Ceramics **3** (1978), 403.

[Hil50] R. Hill, *The mathematical theory of plasticity*, (Oxford:Clarendon) (1950).

[HJW+00] K Herrmann, N.M Jennett, W Wegener, J Meneve, K Hasche, and R Seemann, *Progress in determination of the area function of indenters used for nanoindentation*, Thin Solid Films **377-378** (2000), 394 – 400, International Conference on Metallurgic Coatings and Thin Films.

[HPK+14] K. Herrmann, T. Polzin, M. Kompatscher, R. Mennicke, C. Ullner, and A. Wehrstedt, *Härteprüfung an metallen und kunststoffen*, expert verlag, Reningen, Germany, 2014.

[IB96] A. Iost and R. Bigot, *Indentation size effect: reality or artefact?*, Journal of material Science **31** (1996), 3573–3577.

[ISO08a] ISO/IEC, *Propagation of distributions using a Monte Carlo method*, ISO/IEC 98–3:2008/Suppl 1:2008, International Organization for Standardization, Geneva, Switzerland, 2008.

[ISO08b] ———, *Uncertainty of measurement – part 3: Guide to the expression of uncertainty in measurement (GUM:1995)*, ISO/IEC 98–3:2008, International Organization for Standardization, Geneva, Switzerland, 2008.

[ISO11] ———, *Extension to any number of output quantities*, ISO/IEC 98–3:2008/Suppl 2:2011, International Organization for Standardization, Geneva, Switzerland, 2011.

[ISO15a] *Metallic materials – instrumented indentation test for hardness and materials parameters – part 1: Test method*, ISO 14577–1:2015, International Organization for Standardization, Geneva, Switzerland, 2015.

[ISO15b] *Metallic materials – instrumented indentation test for hardness and materials parameters – part 2: Verification and calibration of testing machines*, ISO 14577–2:2015, International Organization for Standardization, Geneva, Switzerland, 2015.

[JH84] B. Jönsson and S. Hogmark, *Hardness measurements of thin films*, Thin Solid Films **114** (1984), 257–269.

[Joh85] K. L. Johnson, Contact Mechanics, Cambridge University Press (1985).

[JRL89] L. Rosenfeld J.E. Ritter, T. J. Lardner and M.R. Lin, *Measurement of adhesion of thin polymer coatings by indentation*, J.Appl. Phys. (1989).

[Kis86] P. S. Kisly, Inst. Phys. Conf. Ser. **75** (1986), 107.

[KP10] Min-Seok Kim and Jon R. Pratt, *Si traceability: Current status and future trends for forces below 10 micronewtons*, Measurement **43** (2010), no. 2, 169 – 182.

[KPBJ12] Min-Seok Kim, Jon R Pratt, Uwe Brand, and Christopher W Jones, *Report on the first international comparison of small*

force facilities: a pilot study at the micronewton level, Metrologia **49** (2012), no. 1, 70.

[Kul99] K.A.M. Kulisch, *Deposition of diamond-like superhard materials*, Springer, 1999.

[LS92] T.A. Laursen and J. C. Simo, J. Mater. Res. **7** (1992), 618.

[LSK+07] E. D. Langlois, G. A. Shaw, J. A. Kramar, J. R. Pratt, and D. C. Hurley, *Spring constant calibration of atomic force microscopy cantilevers with a piezosensor transfer standard*, Review of Scientific Instruments **78** (2007), no. 9, 093705.

[MA89] H. Shi M. Atkinson, Mater. Sci. Technol. **5** (1989), 613.

[Mar64] D.M. Marsh, Proc. R. Soc.A **279** (1964), 420.

[Mat86] M.J. Matthewson, *Adhesion measurement of thin films by indentation*, Appl. Phys. Lett. **49** (1986), 1426.

[MK96] K. Matsuda and M. Kaneta, *Analysis of the vickers hardness of electroplated coatings*, Phil. Mag. A **74** (1996).

[MM94] Y. Murakami and K. Matsuda, J. Appl. Mech. **61** (1994), 822.

[MN88] M.J. Mayo and W.D. Nix, Acta Met. **8** (1988), 2183.

[MOGC92] R.M. Hooper M.-O. Guillou, J.L. Henshall and G.M. Carte, J. Hard Mater. **3** (1992), 421–434.

[MP13] Andrea Malengo and Francesca Pennecchi, *A weighted total least-squares algorithm for any fitting model with correlated variables*, Metrologia **50** (2013), no. 6, 654.

[NMFB09] V Nesterov, M Mueller, L L Frumin, and U Brand, *A new facility to realize a nanonewton force standard based on electrostatic methods*, Metrologia **46** (2009), no. 3, 277.

[NS96] V. Navrátil and V. Stejskalová, *Microhardness of thin solid films*, Phys. stat. sol. (a) **157** (1996), 339–344.

[OP92a] W. C. Oliver and G. M. Pharr, *An improved technique for determining hardness and elastic-modulus using load and displacement sensing indentation experiments*, J. Mater. Res. **7** (1992), 1564 – 1583.

[OP92b] W.C. Oliver and G.M. Pharr, *An improved technique for determining hardness and elastic modulus using load and displacement sensing indentation experiments*, J. Mater. Res. **7** (1992), 1564.

[PKNS05] Jon R Pratt, John A Kramar, David B Newell, and Douglas T Smith, *Review of si traceable force metrology for instrumented indentation and atomic force microscopy*, Measurement Science and Technology **16** (2005), no. 11, 2129.

[PLLV96] A.E. Giannakopoulos D.J. Rowcliffe P.-L. Larsson, E. Söderlund and R. Vestergaard, Int. J. Solids Struct. **33** (1996), 221.

[SCE82] D.B. Marshall S.S. Chang and A.G. Evans, J. appl. Phys. **53** (1982), 298.

[SD99] J.E. Klemberg-Sapieha S. Dahl, *Nano-scale characterisation of plasma treated polymer surfaces*, Mat. Res. Soc. Symp. **544** (1999), 121–126.

[Sne65] I.N. Sneddon, J.Engin. Sci. **3** (1965), 47.

[SRS+10] Leena Stenlund, Kari Riski, Jeremias SeppÄ¤, Marko Pudas, Mikko VÄ¤hÄ¤sÄ¶yrinki, Ville Tuhkanen, and Juha RÄ¶ning, *Traceable characterization of a bending millimetre scale cantilever for nanoforce sensing*, Measurement Science and Technology **21** (2010), no. 7, 075102.

[SV00] et. al. S. Vepřek, *Composition, nanostructure and origin of the ultrahardness in nc-tin/a- si_3n_4/a - and nc - $tisi_2$ nanocomposites with h_v = 80 to 105 gpa*, Surf. Coat. Technol. (2000).

[SVS95] S. Reiprich S. Vepřek and L. Shizhi, Surf. Coat. Technol. **66** (1995), 2640.

[Tab50] D. Tabor, *The hardness of metals*, (Oxford:Clarendon), 1950.

[TTN99] J. Vlassak T.Y. Tsui and W.D. Nix, J. Mater. Res. **14** (1999), 2204.

[VIM12] *International vocabulary of metrology â€“ basic and general concepts and associated terms (VIM)*, JCGM 200:2012, JCGM, 2012.

[VN93] J.J Vlassak and V.D. Nix, Phil.Mag. A **67** (1993), 1045.

[ZR96] K. Zeng and D.J. Rowcliffe, Philosophical Magazine A **74** (1996).